JOURNAL OF PETROLOGY

Journal of Petrology, 2017, Vol. 58, No. 2, 297–326
doi: 10.1093/petrology/egx017
Original Article

OXFORD

Crystallization of Heterogeneous Pelitic Migmatites: Insights from Thermodynamic Modelling

Brett M. Koblinger* and David R. M. Pattison

Department of Geoscience, University of Calgary, Calgary, AB, T2N 1N4, Canada

*Corresponding author. E-mail: brett.koblinger@gmail.com

Received June 30, 2015; Accepted March 23, 2017

ABSTRACT

Pelitic migmatites are texturally and mineralogically heterogeneous owing to variable proportions of light and dark coloured domains (leucosome and melanosome), the degree to which the two domains are segregated from one another and the variable composition of the leucosome (tonalite–trondhjemite to alkali feldspar granite). We use thermodynamic modelling to (1) provide insights into the variation in leucosome composition and solidification conditions for different melting and crystallization processes and (2) address the practical problem of how to sample heterogeneous migmatites for the purpose of constraining the pressure–temperature conditions of their formation. The latter is challenging because the appropriate bulk composition is affected by the above heterogeneity, as well as by the possibility of melt loss. Both dehydration melting and excess-water melting (for 2·0 wt % excess water) are simulated for both equilibrium and fractional melting end-member processes. Three end-member processes are considered during the crystallization stage: (1) fractional crystallization of the melt; (2) equilibrium crystallization of just the melt in isolation from the solid phases; (3) crystallization during which melt and solids maintain chemical communication. Loss of melt during heating and cooling are also considered. Some of the key results of our simulations of pelitic migmatites are as follows. (1) Leucosome composition is primarily a reflection of the melt composition and to lesser degrees the crystallization process and the temperature of melt loss during cooling. Granite (*sensu stricto*) is the most common leucosome type, arising from many melting and crystallization processes, whereas tonalite or trondhjemite leucosome is generally indicative of excess-water melting. (2) Melts lost from partially molten regions, which have the potential to coalesce and form granites at shallower crustal levels, show less compositional variation than leucosomes in migmatites. Extracted melts are monzogranitic, or rarely granodioritic at low temperatures. (3) Comparing plagioclase compositions between leucosome and melanosome is potentially an effective means of distinguishing between crystallization processes, as well as the degree of retrograde melt–leucosome–melanosome chemical interaction. Fractional crystallization produces zoned plagioclase in the leucosome, isolated equilibrium crystallization produces plagioclase of different composition in the leucosome and melanosome, whereas chemical interaction causes the leucosome and melanosome plagioclase compositions to remain similar during crystallization. (4) The peak temperature of heterogeneous migmatites is most reliably constrained from an equilibrium phase assemblage diagram calculated using just the melanosome composition. Addition of leucosome to the melanosome composition can lead to peak-temperature estimates that differ from actual peak conditions by −25 to +50°C. In extreme cases, such as in rocks containing high proportions of leucosome to melanosome, or in which K-feldspar was absent as a solid phase at peak-temperature conditions, the assemblage developed in the rock at peak temperature may not appear in the phase diagram at all. (5) The solidification temperature (the temperature at which a partially molten rock changes to a completely solid migmatite, owing to either crystallization of the last melt or physical loss of the melt) can be accurately constrained if the melt and solids chemically communicated during cooling. If the melt crystallized in isolation

from the melanosome, the solidification temperature is the temperature at which the last melt was physically lost or that of a water-saturated granitoid solidus (625–645°C). In the latter case, the solidification temperature may be much higher, but can only be estimated with a precision of tens to hundreds of degrees Celsius.

Key words: forward thermodynamic modelling; leucosome composition; migmatite; melt loss; metapelite; fractional crystallization

INTRODUCTION

Migmatites are heterogeneous, high-grade metamorphic rocks produced by the partial melting of a source rock, followed by crystallization of the melt. The heterogeneity of migmatites derives from several factors: variable proportions of light and dark coloured domains (leucosome and melanosome); the degree to which the two domains are segregated from one another; the variable composition of the leucosome, the latter ranging from tonalite–trondhjemite to alkali feldspar granite. Figure 1 illustrates two migmatites, one showing significant segregation of leucosome and melanosome (Fig. 1a), the other a more intimate intermixing of the two (Fig. 1b). Other examples of the diverse textures and structures of these complex rocks can be found in the *Atlas of Migmatites* by Sawyer (2008*a*).

Migmatites are of broad interest because they provide evidence, in their mineralogy, textures and chemical compositions, of the reactions and physical processes involved in the generation and segregation of granitoid magmas that source abundant intrusive and extrusive felsic rocks in the continental crust (Mehnert, 1968; Brown, 1994, 2007, 2013; Brown *et al.*, 2011; Sawyer *et al.*, 2011). In addition, because anatexis involves production of a lower-viscosity liquid phase, small volumes of melt reduce rock strength markedly (Rosenberg & Handy, 2005; Diener & Fagereng, 2014). Partial melting therefore changes the rheological behaviour of the crust, which in turn influences orogenic evolution (e.g. Jamieson & Beaumont, 2013).

Much emphasis has been placed on prograde melting reactions in migmatites (White *et al.*, 2001, 2003, 2004, 2007; Droop & Brodie, 2012; Redler *et al.*, 2013). However, forming a migmatite also requires consideration of the crystallization reactions and processes (Brown, 2002; White *et al.*, 2004; White & Powell, 2010), which take place after the melt has segregated from its source and accumulated in melt-dominated sites (e.g. Stevenson, 1989; Brown, 1994; Sawyer, 1994, 2014; Simakin & Talbot, 2001; Rabinowicz & Vigneresse, 2004). By understanding the crystallization history, the composition of the melt lost from partially molten terrains can be better understood (Johannes *et al.*, 2003; Johnson *et al.*, 2003), and the retrograde solidification

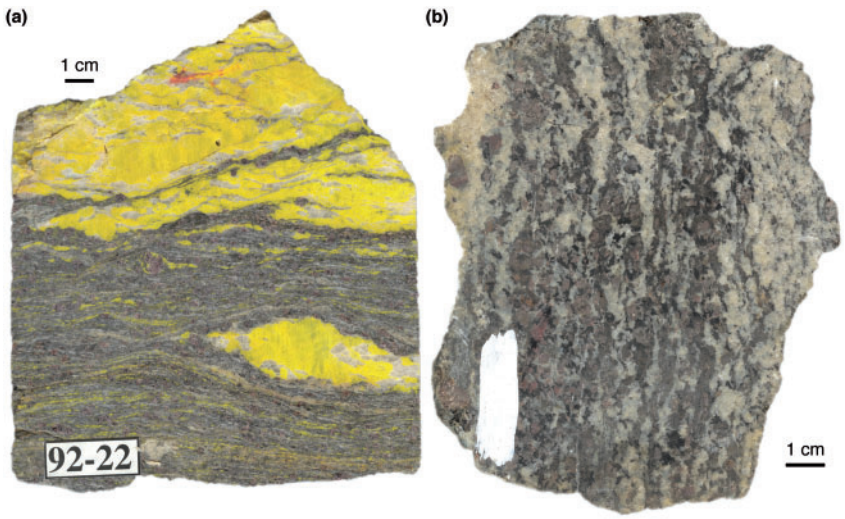

Fig. 1. Photographs of two pelitic migmatites showing stromatic metatexite texture but with different degrees of segregation of leucosome and melanosome. Both samples contain the same mineral assemblage: Bt + Grt + Sil + Kfs + Pl + Qtz. (a) Sample stained with sodium cobaltinitrite to highlight Kfs. Two large leucosomes and numerous thin leucosomes are visible. Deformation features, including ribbon quartz, shear bands and foliation that wraps individual leucosomes, suggest solid-state deformation following crystallization of the leucosome. Whereas the two obvious, larger leucosomes might be separated from the rock for whole-rock geochemical analysis, the millimetre-scale leucosomes would be more difficult to separate from the melanosome. Sample from the Monashee Complex, British Columbia, described by Nyman *et al.* (1995). (b) Sample showing more intimate intermingling of leucosome and melanosome. The thin widths and irregular boundaries between melanosome and leucosome domains would make physical separation of melanosome and leucosome material difficult. Sample from southeastern British Columbia, details unknown.

P–T conditions can be determined. The latter constrains the minimum temperature (*T*) at which weak partially molten rock undergoes a transition to a stronger solid aggregate.

In pelitic migmatites, leucosome compositions are generally granitoid, but they can vary widely from trondhjemite to granite to alkali feldspar granite (e.g. Powell & Downes, 1990; Vernon *et al.*, 2001; Sawyer, 2008*a*). This variation has the potential to provide insights into melting and crystallization processes and the *P–T* conditions at which they occur. In this study, we use thermodynamic forward modelling techniques to simulate prograde melting reactions and develop new modelling techniques to simulate retrograde crystallization in migmatites. We focus on pelitic migmatites, but the method extends to any type of migmatite.

Thermodynamic modelling of migmatites carries special challenges (Brown & Korhonen, 2009; Kelsey & Hand, 2015). The varying proportions of leucosome and melanosome make the equilibrium composition unclear (Fig. 1). The segregation of melt from its source allows the degree of chemical interaction between melt and solids during cooling to vary. The drainage of melt from the source is an open-system process, as is the possible addition of externally derived melt, such as in sills and dikes. We attempt to address these matters with a series of simulations and phase diagram calculations. In the first part of the study, we simulate migmatites that underwent various melting and crystallization processes. We then calculate phase diagrams for the simulated migmatitic rocks and use the phase diagram mineral assemblage fields to estimate *P–T* conditions. Our main findings pertain to interpreting leucosome compositions, devising strategies for interpreting and modelling heterogeneous migmatites, and constraining the peak and solidification *P–T* conditions of migmatites.

OVERVIEW OF MELTING AND CRYSTALLIZATION SIMULATIONS

Our migmatite simulations consist of a combination of prograde melting and retrograde crystallization simulations. Our approach is to understand the end-member processes involved in the evolution of migmatites; natural migmatites are probably a result of some combination of these end-member processes. In this section, we introduce the protolith and *P–T* paths for the simulations, as well as the melting and crystallization processes. All the simulations are summarized in Table 1. Details of the method are described in more detail in subsequent sections.

Protolith

A single protolith composition, here termed the source, was used for this study: the average composition of amphibolite-facies, muscovite-bearing metapelitic schist from the *c.* 2·0 Ga Hoare Bay group (currently informally defined), southeastern Baffin Island, Nunavut, Canada

Table 1: Overview of the melting and crystallization models

Scenario:	Scenario A				Scenario B				Scenario C					
Melting model:	Equilibrium		Fractional		Equilibrium		Fractional		Equilibrium		Fractional		Prograde melt loss	
Melting simulation abbrev.:	AE		AF		BE		BF		CE		CF		CP	
Melting figures	3a, b		3c		3e, f		3g		3i, j		3k		3l	
Crystallization model:	Isolated fract.	Isolated equil.	Chemical int.	Isolated fract.	Isolated equil.	Chemical int.	Isolated fract.	Isolated equil.	Isolated fract.	Isolated equil.	Chemical int.	Isolated fract.	Isolated equil.	Chemical int.
Crystallization simulation abbrev.:	AEF	AEE	AEI	AFF	AFE	BEF	BEE	BEI	BFF	BFE	CEF	CEE	CEI	CFF	CFE	CPF	CPE	CPI
Crystallization figures	A2a	A2b	5, A2c	A2d	A2e	6a	6b	6c, A1a–d	6d	6e	6f	6g	6h, A1e–g	A2f	A2g	6i	6j	6k, A1h–k
Heterogeneity sampling experiment figures	8a, A4a–c		A4v–x	A4j–l			A4d–f	8e, A4y–aa	8c, A4m–o			8b, A4g–i	8f, A4bb–dd	A4p–r		8d, A4s–u		A4ee, ff

fract, fractional; equil, equilibrium; int, interaction. Figure numbers with prefix 'A' are Supplementary Data figures.

(Supplementary Data Table A1, available for downloading at http://www.petrology.oxfordjournals.org; Sanborn-Barrie *et al.*, 2013). These schists have the mineral assemblage Qtz + Bt + Ms + Sil ± Pl ± And ± St + Ilm [mineral abbreviations according to Whitney & Evans (2010)], and have been shown to pass upgrade into a terrain of migmatites (Hamilton *et al.*, 2012). The composition of the average Hoare Bay group metapelite is similar to the average composition of pelites reported in the literature (Cameron & Garrels, 1980; Gromet *et al.*, 1984; Taylor & McLennan, 1985; Ague, 1991), but is slightly more aluminous and less magnesian (Supplementary Data Table A1).

Pressure (*P*)–temperature (*T*) paths

Simulations consider two isobaric *P*–*T* paths that produce commonly observed mineral assemblages in the Hoare Bay group pelitic migmatites (Hamilton *et al.*, 2012). One path is for typical mid-crustal upper amphibolite-facies, Kfs + Sil zone conditions at 6·5 kbar, extending to 800°C (Fig. 2). The other *P*–*T* path enters the Crd + Grt stability field and extends to high-*T* granulite-facies conditions at 920°C at 5·3 kbar (Fig. 2). The latter were chosen to produce Crd-bearing assemblages, which are common in many regional migmatite terranes, and a peak-*T* Qtz + Spl assemblage in which all of the Kfs dissolves into the melt. For simplicity, we consider just isobaric heating and cooling, which allows us to eliminate some variables in an already complex modelling exercise (see Yakymchuk & Brown, 2014).

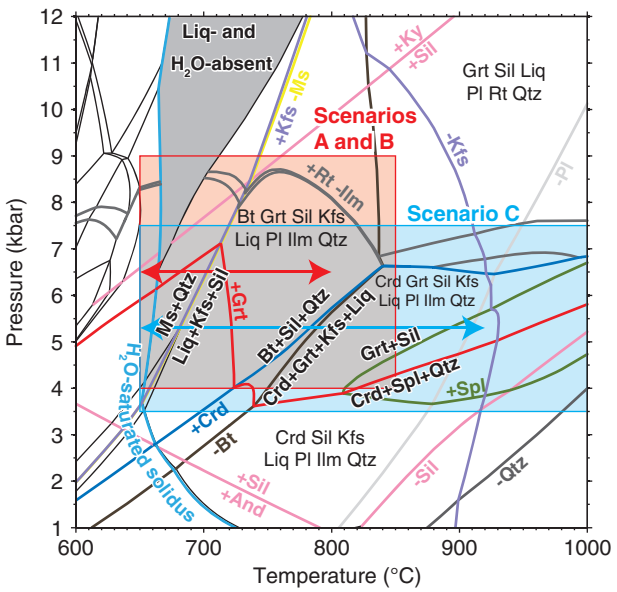

Fig. 2. Overview phase diagram calculated for the bulk composition of scenario A (Supplementary Data Table A2). Coloured text labels indicate phase boundaries, bold black text labels significant low-variance reactions, and smaller black text labels are for selected assemblages. The arrows are the *P*–*T* paths of simulation scenarios A and B (red), and C (blue; see text for details). The shaded boxes show the comparative position of the *P*–*T* diagrams in subsequent figures.

Fluid during melting

Two end-member processes are commonly cited in the literature: dehydration melting and fluid-saturated melting. During dehydration melting, there is no free fluid, but H_2O dissolves into the melt during the breakdown of hydrous minerals, such as Ms or Bt, for the pelites investigated here. During fluid-saturated melting, a free hydrous fluid is a reactant and is always present in excess. A growing body of literature suggests that an intermediate behaviour may be common, in which some H_2O infiltrates partially molten rocks, but is insufficient to saturate the system in H_2O during all melting reactions (Weinberg & Hasalová, 2015, and references therein). The quantities of H_2O estimated to have infiltrated supra-solidus pelites range from 0·8 to 5·5 wt % (Johnson *et al.*, 2001; Otamendi & Patiño Douce, 2001; White *et al.*, 2005; Genier *et al.*, 2008; Ward *et al.*, 2008; Braga & Massonne, 2011). Jung *et al.* (2000) and Droop & Brodie (2012) concluded that an aqueous fluid infiltrated at temperatures slightly above the solidus. Although many fluid behaviours intermediate between dehydration melting and fluid-saturated melting are possible, here we concern ourselves with what we term excess-water melting. During excess-water melting, a small amount of free H_2O saturates the rock at the solidus. As a result, fluid-saturated melting reactions first consume the free H_2O fluid phase and are followed by dehydration melting reactions.

Both dehydration melting and excess-water melting are simulated. During simulations of dehydration melting, only a trivial amount of free H_2O is present in the composition immediately down-*T* of the water-saturated solidus. During simulations of excess-water melting, we allow 2 wt % free H_2O to remain in the bulk composition immediately down-*T* of the water-saturated solidus.

For the above combinations of *P*–*T* path and fluid behaviour, three prograde scenarios reveal the range of possible outcomes (Table 1). Scenario A involves dehydration melting along the 6·5 kbar, amphibolite-facies *P*–*T* path. Scenario B involves excess-water melting along the same amphibolite-facies *P*–*T* path. Scenario C involves excess-water melting along the 5·3 kbar, granulite-facies *P*–*T* path. Fractional and equilibrium melting are simulated for each of the scenarios. We chose to model excess-water melting only for the amphibolite-facies *P*–*T* path. Fluxing H_2O into a rock at temperatures well above its solidus is probably only possible if the H_2O is part of a hydrous melt (Weinberg & Hasalová, 2015) and is beyond the scope of the study.

Melt generation and crystallization

Partial melting creates a new phase with a lower density and viscosity than the coexisting solids. This liquid segregates from the source to varying degrees, as manifested by quartzofeldspathic leucosomes, granitoid veins, and larger granitoid bodies (Fig. 1). Segregation is thought to be possible only after a certain volume of melt accumulates along grain boundaries. This is called

the liquid percolation threshold (Vigneresse *et al.*, 1996), with estimates of the threshold ranging from about 1 vol. % (Rosenberg & Handy, 2001) to 8 vol. % (Vigneresse *et al.*, 1996) melt. The degree to which the melt and the residuum, from which the melt was extracted, maintain chemical equilibrium during melting and crystallization probably varies. Many migmatitic rocks contain a relatively anhydrous mineral assemblage, in some instances with minimal evidence of retrogression, consistent with melt loss (Powell, 1983; Waters, 1988; Powell & Downes, 1990; Carson *et al.*, 1997; White *et al.*, 2001; White & Powell, 2002; Guernina & Sawyer, 2003; Ward *et al.*, 2008; Morfin *et al.*, 2014). Both melt segregation, the physical separation of melt from the source into a melt-dominated domain near the site of melting, and melt loss, the complete extraction of the melt from the vicinity of the site of melting such that crystallization occurs at a different crustal level, are probably controlled by physical processes (e.g. Rutter & Mecklenburgh, 2006).

The degree of interaction between melt and residuum also probably varies during cooling and crystallization. Minerals in the melanosome and leucosome commonly have similar compositions, especially plagioclase (Misch, 1968; Gupta & Johannes, 1982; Johannes & Gupta, 1982; Powell & Downes, 1990; Johannes *et al.*, 1995, 2003; Jung *et al.*, 1998; Marchildon & Brown, 2001; Harris *et al.*, 2004; Genier *et al.*, 2008), suggesting that the residuum, melt, and crystallized solids chemically interacted during cooling (Fourcade *et al.*, 1992; Nabelek, 1999; Kriegsman, 2001). However, leucosome plagioclase is zoned in some migmatites (e.g. Holness & Sawyer, 2008) suggesting limited interaction of the melt and residuum.

Although melt loss during melting, here called prograde melt loss, has been the focus of many studies, melt loss during cooling, here called retrograde melt loss, also needs to be considered because the physical driving forces for expulsion may persist during cooling (White & Powell, 2010; Carvalho *et al.*, 2016). White & Powell (2010) suggested that retrograde melt loss is most likely to occur when the leucosome is composed of 20–55 vol. % liquid, as the leucosome changes rheologically from behaving like a liquid to behaving like a solid, passing through the rigid percolation threshold (Vigneresse *et al.*, 1996) or the solid-to-liquid transition (Rosenberg & Handy, 2005). This hypothesis is supported by petrographical and geochemical studies suggesting that some leucosomes represent cumulates after the more evolved liquid was lost (Sawyer, 1987; Ellis & Obata, 1992; Fourcade *et al.*, 1992; Milord *et al.*, 2001; Solar & Brown, 2001; Johnson *et al.*, 2003; Slagstad *et al.*, 2005; Cruciani *et al.*, 2008; Daczko & Halpin, 2009; Morfin *et al.*, 2014; Brown *et al.*, 2016).

Prograde melt behaviour (melting)

Prograde melt simulations give rise to residuum and melt compositions that are used later in the crystallization step. Prograde simulations consider two end-member processes (Table 1): equilibrium melting with continual prograde chemical equilibration between melt and solid phases and fractional melting where the melt does not chemically interact with the residuum after it is produced. In both equilibrium and fractional melting, melt is assumed to segregate from the residuum, forming melt-only domains that will later crystallize into leucosome. A third case, prograde melt loss, involves a portion of early formed melt being lost from the system, followed by equilibrium melting [similar to models suggested by Kriegsman (2001) and Yakymchuk & Brown (2014)].

Retrograde melt behaviour (crystallization)

Melt is simulated to crystallize via one of three end-member processes (Table 1): (1) isolated fractional crystallization of just the melt; (2) isolated equilibrium crystallization of just the melt; (3) a crystallization process called chemical interaction crystallization that attempts to reproduce the main characteristics of equilibrium crystallization, in which the segregated melt and the solid residuum maintain chemical communication during cooling and crystallization. The models are described in more detail below. All simulations also consider the loss of melt during retrograde crystallization.

THERMODYNAMIC METHODS

Thermodynamic calculations were performed in the chemical system MnO–Na_2O–CaO–K_2O–FeO–MgO–Al_2O_3–SiO_2–H_2O–TiO_2 (MnNCKFMASHT). The whole-rock composition, determined by X-ray fluorescence analysis, was reduced to MnNCKFMAST by projecting from apatite [$Ca_5(PO_4)_3(OH)$] and pyrrhotite (FeS), and neglecting all other components (Supplementary Data Table A1). Bulk-rock H_2O content is manipulated in the simulations, as described below.

Calculations use an updated version of the Holland & Powell (1998) thermodynamic dataset (version 5.5, November 2003) and mineral activity–composition models applicable to pelites at supra-solidus conditions (White *et al.*, 2007): ternary feldspar with $C\bar{1}$ structure (Holland & Powell, 2003), biotite (White *et al.*, 2007), garnet [the 'currently preferred model' downloaded from the THERMOCALC website on September 25, 2013 updated from White *et al.* (2007) with the modifications $W_{Alm,Grs} = 10$ kJ mol^{-1}, $W_{Prp,Grs} = 45$ kJ mol^{-1}, and $\alpha_{Grs} = 3$], cordierite, staurolite, and chloritoid (Holland & Powell, 1998), spinel (White *et al.*, 2002), orthopyroxene (Powell & Holland, 1999; White *et al.*, 2002), muscovite (Coggon & Holland, 2002), ilmenite [White *et al.* (2005), with $W_{oilm1,pnt} = 0$ kJ to prevent anti-ordered ilmenite; D. Tinkham, personal communication, 2012], and silicate liquid (Holland & Powell, 2001; White *et al.*, 2001, 2007). The activity–composition models for garnet, biotite, chlorite, cordierite, staurolite, and chloritoid were expanded into the Mn-bearing subsystem to stabilize

Grt to lower *P* and *T* following Tinkham *et al.* (2001) and Stowell *et al.* (2011). The software Theriak/Domino (de Capitani & Brown, 1987; de Capitani & Petrakakis, 2010), based on free energy minimization, was used to perform all equilibrium calculations and MATLAB scripts were used to perform ancillary calculations.

PROGRADE MELTING SIMULATIONS

Seven prograde melting simulations were calculated to cover the possibilities described above (Table 1). Dehydration melting (scenarios A and C) is simulated by fixing bulk H_2O as the H_2O in the hydrous phases calculated for an H_2O-saturated composition 0·5°C below the water-saturated solidus at the pressure of the simulations (6·5 kbar for scenario A and 5·3 kbar for scenario C). This simulates a source with a vanishingly small amount of aqueous fluid along grain boundaries near its solidus. Excess-water melting (scenario B) is simulated by increasing H_2O in the bulk composition for scenario A by 2·0 wt %. After this free water is consumed, dehydration melting takes over. Compositions of the source, melt, and residuum are provided in Supplementary Data Table A2.

During both equilibrium and fractional melting, the melt is assumed to physically segregate from the solids (residuum) and pool, forming melt-only domains of aggregate melt. In the equilibrium melting simulations, residuum and melt remain in equilibrium and the bulk composition remains constant (simulations AE, BE, and CE, with the E standing for equilibrium melting). In the fractional melting simulations, residuum and melt are treated as separate systems (simulations AF, BF, and CF, with the F standing for fractional melting). Fractional melting is simulated by chemically separating all melt from the residual solids after each 0·5°C increase in *T*. Each small batch of removed melt is added to the aggregate melt, which later crystallizes during cooling. For simplicity, melt is extracted from the residuum as soon as it forms (every 0·5°C; i.e. the liquid percolation threshold is zero) and the process is assumed to be completely efficient (no entrained solids or peritectic phases; see Stevens *et al.*, 2007).

Prograde melt loss is simulated for scenario C only, for simplicity, as follows (called simulation CP): fractional melting occurs to 857°C, with all of the melt produced in this interval being completely lost (every 0·5°C); then equilibrium melting with a retained aggregate melt follows to peak *T*. The peak-*T* aggregate melt crystallizes to form leucosome during the subsequent crystallization simulations. The transition from fractional to equilibrium melting was chosen to be 857°C because a significant amount of melt, 17 vol. % of the source, is produced and lost during melting up to 857°C, satisfying the requirement of significant prograde melt loss. Further melting in the interval from 857°C to the peak *T* of 920°C results in a partially molten rock composed of 6 vol. % melt at peak *T*, a melt volume sufficient to form readily identifiable leucosome in an outcrop. In the spirit of treating end-member processes, our modelling assumes continuous (albeit discretized) and completely efficient fractionation of melt and loss of melt. In nature, however, melt is probably lost in pulses, after a specific volume of melt has accumulated along grain boundaries and is squeezed out of the residuum in response to deformation (Rabinowicz & Vigneresse, 2004). Natural migmatites, with all their diversity, are therefore expected to form in a manner intermediate to our simulations.

Equilibrium mineral assemblages and prograde reactions for the different melting simulations are depicted on *P*–*T* phase diagrams and on plots showing the variation with *T* of mineral mode, melt mass per cent and H_2O content of the melt (Fig. 3). For each simulation, the bulk composition of the source and the evolving composition of both the melt and solid residuum are recorded at a series of temperatures (Supplementary Data Table A2). The evolving melt compositions are plotted on Qtz–Kfs–Pl ternary diagrams (herein termed QAP diagrams) calculated from CIPW norms (Fig. 4b; Cross *et al.*, 1903; Le Maitre, 2002). Because the CIPW norm does not consider the hydrous and potassic phases Ms and Bt, nor many common solid solutions, such as the substitution of Na for K in Kfs, the CIPW norm is slightly different from the mineralogy of a rock with the same composition. For the granitoids considered here, normative Kfs is typically overestimated and normative Qtz is underestimated.

Melting reactions

Prograde melting reactions were determined by calculating the change in the molar abundance of each mineral and melt for every temperature increment. The reactions include only those phases being consumed and those being produced, but not the change in the composition of the phases, making them simplified net reactions. All of the reactions determined are listed in Table 2 and the *T* interval of each reaction is indicated in the phase diagrams (Fig. 3a, e and i). In all simulations, melt is produced by high-variance reactions that consume mainly Qtz + Pl ± Kfs ± Bt over broad *T* intervals, alternating with lower-variance reactions that produce significant quantities of melt over smaller *T* intervals. The reaction sequence depends primarily on the *P*–*T* path, but is also influenced by the simulated prograde processes (e.g. equilibrium vs fractional melting).

In both of the melting simulations for scenario A (equilibrium AE and fractional AF; Fig. 3a–c) a trivial amount of silicate liquid is produced by the dissolution of grain-boundary water at the water-saturated solidus (664°C at 6·5 kbar). A small amount of silicate liquid is produced by the continuous dissolution of Ms at higher *T* by reactions 2–3 (Table 2), until Kfs is produced at 702°C by muscovite dehydration melting (reaction 4), resulting in the peak-*T* assemblage Bt + Grt + Sil + Kfs + Pl + Ilm + Qtz + Liq. Thereafter, melt is continuously produced by the dehydration melting of Bt in this

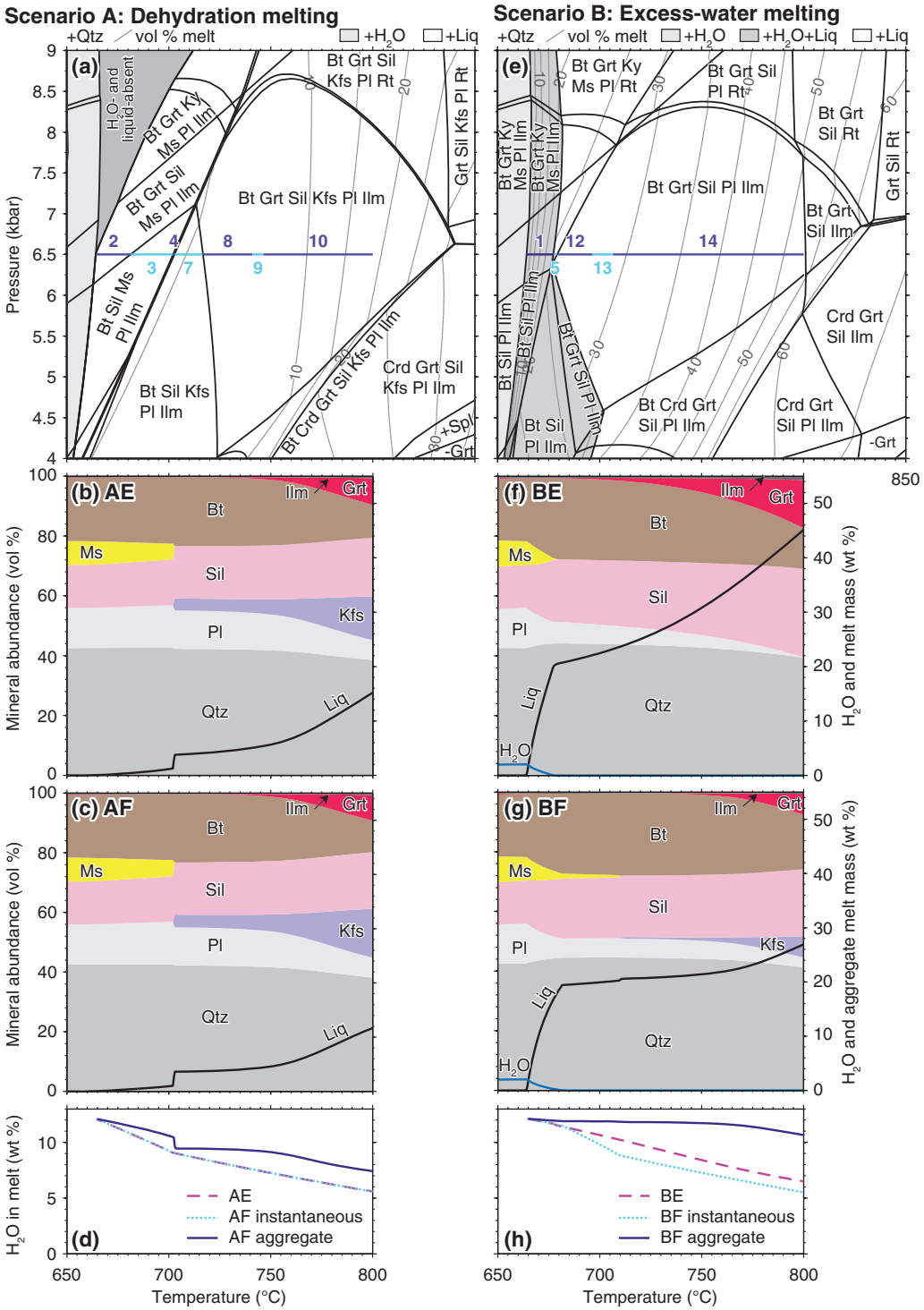

Fig. 3. (a, e, i) Phase diagrams for melting simulations for scenarios A, B and C, respectively, with vol. % melt contours. Two-tone blue lines denote the different net reactions along the prograde *P*–*T* paths for equilibrium melting simulations; numbered labels correspond to reaction numbers in Table 2. (b, f, j) Mineral modes and melt abundance along the prograde *P*–*T* paths for the three melting simulations assuming equilibrium melting. (c, g, k) Mineral modes and melt abundance along the prograde *P*–*T* paths for the three melting simulations assuming fractional melting. (l) Mineral modes and melt abundance along the prograde *P*–*T* path of melting simulation CP assuming prograde melt loss. (d, h, m) Amount of H_2O in the melt along the prograde path for simulations of equilibrium melting, fractional melting and melting with prograde melt loss. For fractional melting simulations, the composition of the melt is plotted both as the small batch of melt produced during each 0·5°C *T* increment (instantaneous), and the combination of all melt produced up to the given *T* (aggregate). For equilibrium melting simulations, the instantaneous and aggregate melt compositions are the same.

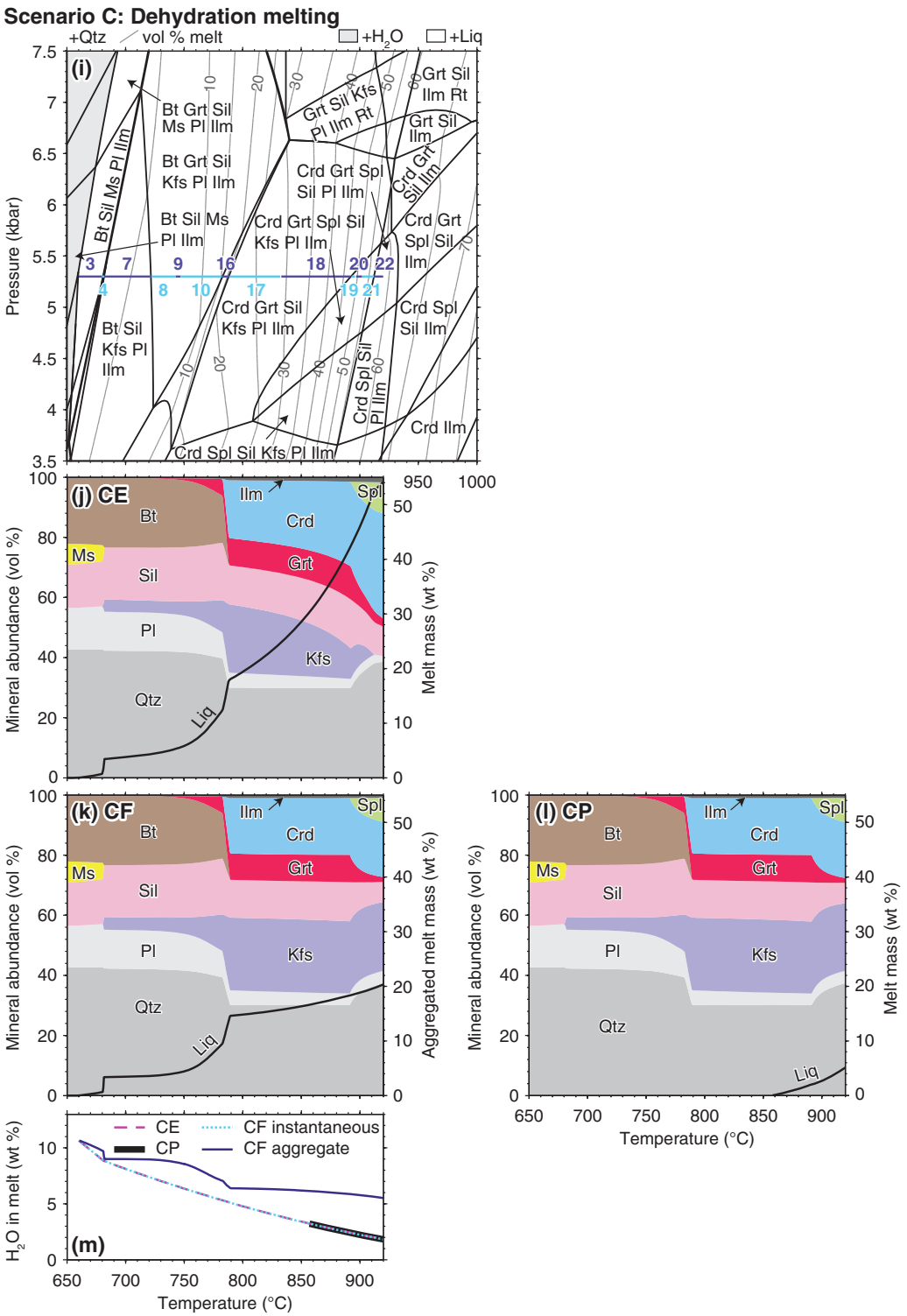

Fig. 3. Continued

assemblage (reactions 7–10 in simulation AE and reactions 8–11 in simulation AF). Biotite dehydration melting (reactions 7–11) produces the majority of the melt in both AE and AF simulations. By 800°C, reactions 7–11 produce 11 wt % of the 15 wt % melt produced in simulation AE and 8 wt % of the 12 wt % melt produced in simulation AF.

In simulations of scenario B, which underwent excess-water melting, the mineral assemblage sequence is different, and a greater amount of melt is produced (Fig. 3e–h) compared with simulations of dehydration melting. Melting begins at the water-saturated solidus (664°C at 6·5 kbar) with water-saturated melting (reaction 1). As *T* increases, the

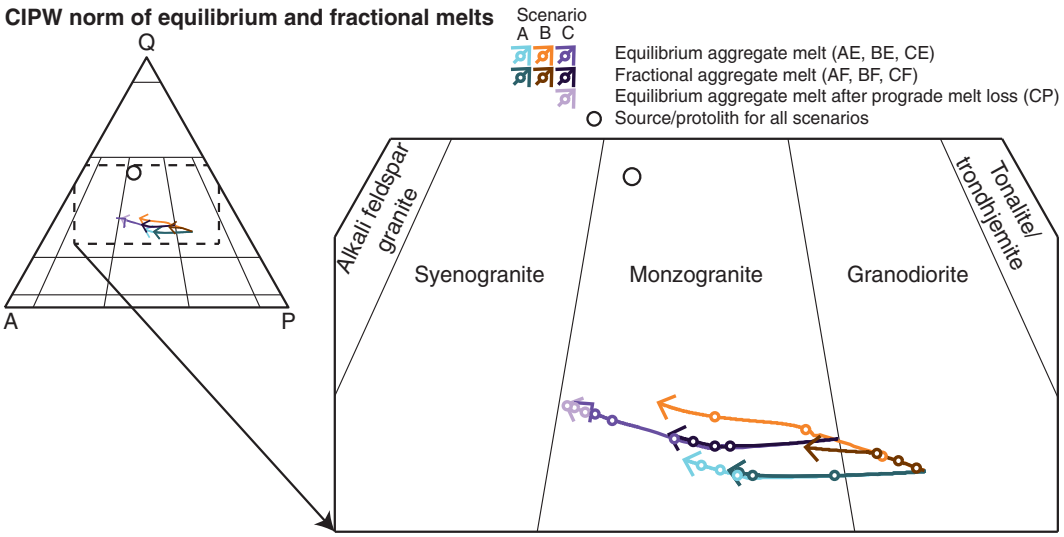

Fig. 4. Modal CIPW normative compositions of melt and protolith for the melting simulations described in the text, plotted on a quartz–alkali feldspar–plagioclase (QAP) ternary diagram. Each arrow points in the direction of increasing *T* and tracks the evolving melt composition. The small circles along the arrows correspond to compositions in Supplementary Data Table A2 and the large circle is the protolith composition.

Table 2: Prograde melting reactions for all melting simulations

Water-saturated melting			
(1)	$H_2O + Ms + Qtz + Pl + Grt + Ilm$	=	$Liq + Sil + Bt$
Muscovite dehydration melting reactions			
(2)	$Ms + Qtz + Grt + Ilm$	=	$Liq + Pl + Sil + Bt$
(3)	$Ms + Qtz + Ilm$	=	$Liq + Pl + Sil + Bt$
(4)	$Ms + Qtz + Pl + Ilm$	=	$Liq + Kfs + Sil + Bt$
(5)	$Ms + Qtz + Pl + Grt + Ilm$	=	$Liq + Sil + Bt$
(6)	$Ms + Grt + Ilm$	=	$Liq + Qtz + Pl + Sil + Bt$
Biotite dehydration melting reactions			
(7)	$Bt + Qtz + Pl + Kfs + Ilm$	=	$Liq + Sil$
(8)	$Bt + Qtz + Pl + Ilm$	=	$Liq + Kfs + Sil + Grt$
(9)	$Bt + Qtz + Pl$	=	$Liq + Kfs + Sil + Grt + Ilm$
(10)	$Bt + Qtz + Pl + Sil$	=	$Liq + Kfs + Grt + Ilm$
(11)	$Bt + Qtz + Pl + Ilm$	=	$Liq + Kfs + Sil$
(12)	$Bt + Qtz + Pl + Ilm$	=	$Liq + Sil + Grt$
(13)	$Bt + Qtz + Pl + Sil + Ilm$	=	$Liq + Grt$
(14)	$Bt + Qtz + Pl + Sil$	=	$Liq + Grt + Ilm$
(15)	$Bt + Qtz + Pl$	=	$Liq + Kfs + Sil + Ilm$
Cordierite + garnet-producing reactions (biotite dehydration melting)			
(16)	$Bt + Qtz + Pl + Sil$	=	$Liq + Kfs + Crd + Grt + Ilm$
Feldspar + sillimanite melting			
(17)	$Qtz + Pl + Kfs + Sil + Grt$	=	$Liq + Crd$
(18)	$Qtz + Pl + Kfs + Sil + Crd + Grt$	=	Liq
(19)	$Kfs + Sil + Grt + Ilm$	=	$Liq + Qtz + Pl + Crd + Spl$
(20)	$Kfs + Pl + Sil + Crd + Grt + Ilm$	=	$Liq + Qtz + Spl$
(21)	$Qtz + Pl + Kfs + Sil + Crd + Grt + Ilm$	=	$Liq + Spl$
(22)	$Qtz + Pl + Sil + Grt + Ilm$	=	$Liq + Crd + Spl$
(23)	$Qtz + Pl + Sil + Grt$	=	$Liq + Kfs + Crd$
(24)	$Qtz + Pl + Kfs + Sil + Crd$	=	$Liq + Grt$
(25)	$Qtz + Pl + Kfs + Crd$	=	$Liq + Sil + Grt$
(26)	$Kfs + Sil + Crd + Grt + Ilm$	=	$Liq + Qtz + Pl + Spl$

reaction sequence differs for the equilibrium (BE) and fractional (BF) melting simulations. In simulation BE, H_2O is first consumed by reaction 1 at 678°C and then Ms is consumed by muscovite dehydration melting (reaction 5) at 680°C, producing the mineral assemblage $Bt + Grt + Sil + Pl + Ilm + Qtz + Liq$. This Kfs-absent mineral assemblage persists to peak *T* at 800°C and experiences further biotite dehydration melting reactions (reactions 12–14). Of the 45 wt % melt produced at 800°C, both water-saturated melting (reaction 1; 20 wt %) and biotite dehydration melting (reactions 12–14; 25 wt %) produce significant amounts of melt.

In simulation BF, H_2O reacts out via water-saturated melting (reaction 1) at 682°C, followed by muscovite dehydration melting (reaction 6 then 3). K-feldspar and melt are produced as Ms reacts out (710–711°C) via reaction 4. The continued increase in *T* produces additional Kfs and melt via the breakdown of Bt (reactions

8–11 and 15). The peak assemblage is Bt + Grt + Sil + Kfs + Pl + Ilm + Qtz + Liq. Of the 27 wt % melt produced by 800°C, the majority is produced by water-saturated melting (reaction 1; 19 wt %), and biotite dehydration melting (reactions 8–11 and 15; 6 wt %).

For the dehydration melting simulations of scenario C, melting first occurs via muscovite dehydration melting (reactions 3–4) followed by biotite dehydration melting (reactions 7–11), similar to the reaction sequences for scenario A. At 782–789°C (5·3 kbar), a large amount of melt is produced as Crd reacts in and Bt reacts out by reaction 16. Feldspars and Sil dissolve into the increasingly dry melt as *T* increases to the peak *T* (920°C, 5·3 kbar; reactions 17–22 for simulation CE, and reactions 17–20 and 23–26 for simulations CF and CP). In the equilibrium melting case (CE), reaction 21 exhausts Kfs at 913°C and produces the peak-*T* assemblage Crd + Grt + Spl + Sil + Pl + Ilm + Qtz + Liq. In the fractional melting (CF) and prograde melt loss cases (CP), Kfs is not exhausted and the peak assemblage at 920°C contains Kfs. In simulation CE, much of the 54 wt % melt present at 920°C is produced by the dissolution of feldspars and Sil into an increasingly anhydrous melt (reactions 17–20; 24 wt %), whereas in simulation CF, the dehydration melting of Bt (reactions 8–11; 6 wt %) and the melting of feldspars and Sil (reactions 17–20 and 23–26; 5 wt %) produce most of the 20 wt % melt at 920°C.

Melt composition

Effect of P–T *path on melt composition*

The melt composition depends on the *P–T* path and the melting processes. The first-formed melt in simulations of scenarios A and B has the same composition, with a granodiorite CIPW norm, whereas the first-formed liquid in scenario C is less hydrous with slightly more normative Kfs (monzogranite; Fig. 4). In all simulations, as *T* increases, the melt becomes drier and the amount of normative Kfs increases relative to normative Pl. The equilibrium or aggregate melt at peak *T* has a monzogranite norm in all simulations, with the melt at high *T* in scenario C simulations being the most potassic.

Effect of equilibrium vs fractional melting on melt composition

At the solidus, melts produced by equilibrium melting and continuous fractional melting have the same composition. As *T* increases and melting continues, equilibrium aggregate melts become drier and contain more normative Kfs than aggregate fractional melts. Fractional melt simulations produce a smaller volume of aggregate melt compared with equilibrium simulations (Fig. 3b–c, f–g and j–k) because the melt-depleted composition produces less melt than the original source composition (e.g. Patiño Douce & Johnston, 1991; Yakymchuk & Brown, 2014). Consequently, the aggregated fractional melt contains a large proportion of hydrous, granodiorite-normative melt produced at lower *T*.

Effect of dehydration melting vs excess-water melting on melt composition

Melts produced in simulations of excess-water melting (BE and BF) are more hydrous than their counterparts for dehydration melting (AE and AF), as expected (Fig. 3d and h). Simulations of excess-water melting produce a large amount of melt at temperatures just above the water-saturated solidus as H_2O is consumed, giving rise to a low-*T* granodiorite-normative melt that is relatively hydrous (Figs 3 and 4). How the melt composition changes after H_2O is consumed depends on the melting process. In simulation BF, heating to peak *T* consumes relatively little Bt and produces little additional melt. The peak-*T* aggregate melt has a monzogranite composition with the most normative Pl of all simulated peak-*T* melts (Fig. 4). In simulation BE, sufficient Bt is consumed via biotite dehydration melting reactions 12–14 that the melt composition increases in normative Kfs relative to normative Pl and the peak-*T* melt is more hydrous and contains more normative Kfs than in the simulation of dehydration melting (AE).

Effect of prograde melt loss on melt composition

During prograde melt loss (CP), the early formed hydrous, granodiorite-normative melt is lost from the system, resulting in subsequent production of relatively anhydrous, monzogranite melt from melting of the residuum. Although this melt composition is the most anhydrous and contains the most normative Kfs of all the simulated melts, it is nevertheless similar in composition to the equilibrium simulation (CE) melt.

Summary of melting simulation results

The above simulations show variability of melt composition as a result of changing *T*, *P*, bulk H_2O and melting processes. Overall, there is a relatively limited variation in aggregate melt compositions, from normative granodiorite to monzogranite. The most hydrous melts (12·1 wt % H_2O), of granodiorite composition, are produced in small volumes at temperatures slightly above the water-saturated solidus, and in larger volumes at low *T* by excess-water fractional melting (BF). The driest melts (1·8 wt % H_2O), of monzogranite composition, are produced at the highest temperatures via equilibrium melting (CE), or melting following prograde melt loss (CP). The largest amounts of melt are produced either by equilibrium melting to high peak temperatures (CE; 59 wt % melt), or via excess-water melting (BE; 45 wt % melt). Apart from the simulation involving prograde melt loss (CP), fractional dehydration melting produces the smallest aggregate volume of melt at peak *T* (AF; 12 wt % melt).

MELT CRYSTALLIZATION

The formation of most leucosomes in migmatites requires melt crystallization (see Johannes *et al.*, 2003). Three end-member crystallization processes are considered to explore the effects of crystallization on

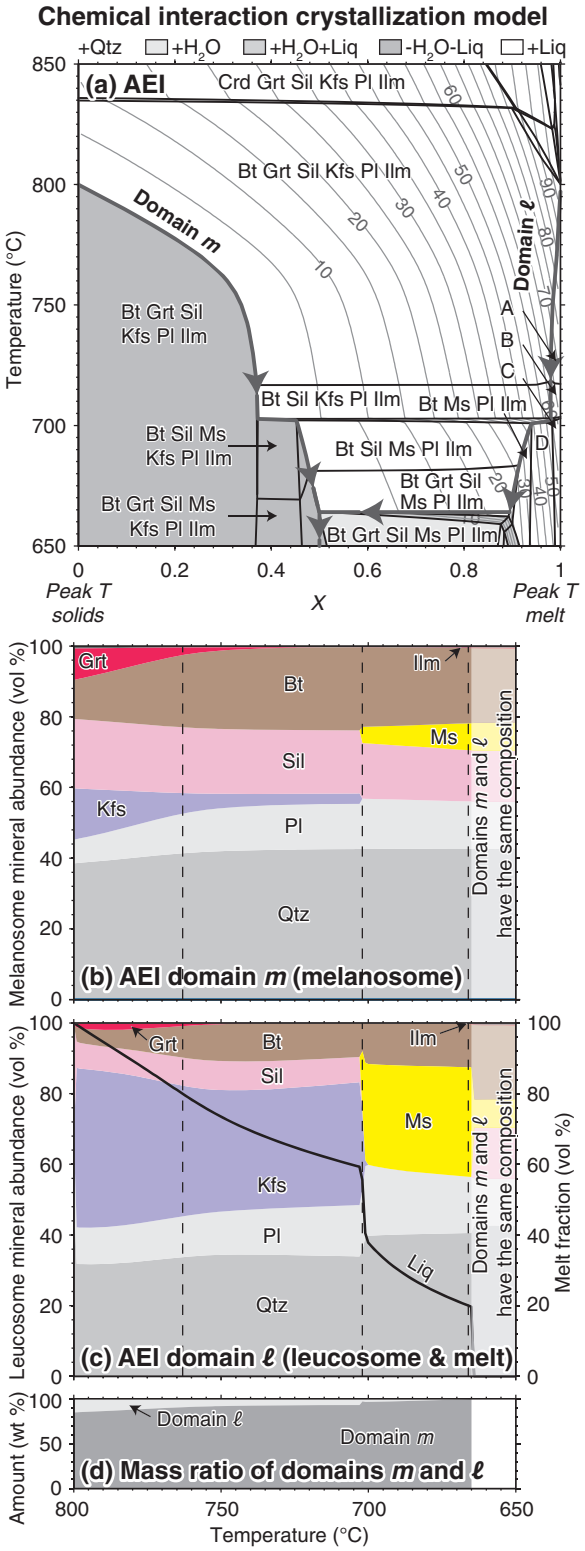

Fig. 5. Chemical interaction crystallization simulation AEI. (a) *T*–*X* phase diagram, where $X=0$ is the composition of the residuum solids and $X=1$ is the composition of the melt at peak *T* following equilibrium melting. Contours are of volume per cent liquid. The two thick grey lines show the evolution of domain *m*, which becomes the melanosome, and domain ℓ, which begins as melt and from which the leucosome solids crystallize, as the system cools and crystallizes: mass transfer moves the composition of the two domains towards one another if ever both domains develop different mineral assemblages (see text for details; A, Bt + Grt + Sil + Kfs + Pl; B, Bt + Sil + Kfs + Pl; C, Bt + Kfs + Ms + Pl; D, Bt + Kfs + Ms + Pl + Ilm). (b) Modal mineralogy of domain *m*. (c) Modal mineralogy of domain ℓ. The compositions of the melanosome and leucosome solids after about 80, 50, and 20 wt % crystallization of the melt, at the temperatures of the vertical dashed lines in (b) and (c), are recorded in Table 3 and Supplementary Data Table A3. (d) Proportion of mass in domains *m* and ℓ.

leucosome mineralogy (Table 1). The first two processes consider equilibrium and fractional crystallization of melt that is chemically isolated from the enclosing residuum, isolated equilibrium crystallization (IEC) and isolated fractional crystallization (IFC), respectively. During IFC, crystallized solids are continuously extracted from the melt, forming leucosome and changing the bulk composition of the melt. During IEC, the melt continues to react with the early crystallized minerals throughout crystallization. The third process, termed chemical interaction crystallization (CIC) simulates the chemical interaction of melt, leucosome and melanosome during cooling. Retrograde melt loss, as considered in this study, refers to the physical loss of all melt at a given *T*, at which point crystallization ceases. The leucosome is that which crystallized up to the point of melt loss.

Crystallization simulations

For IEC and IFC simulations, each of the seven peak-*T* melts produced in the melting section is used as a starting composition (aggregate melts from simulations AE, AF, BE, BF, CE, CF and CP). For the CIC simulations, only simulations in which the melt was in equilibrium with the solids at peak *T* were used as starting compositions (AE, BE, CE and CP). The evolving leucosome compositions during each of the above 18 crystallization simulations are illustrated in Figs 5 and 6 and Supplementary Data Figs A1 and A2. The calculation of CIC simulation AEI is depicted in Fig. 5 and discussed below. The leucosome mineralogy of a representative set of simulations is shown in Fig. 6; the results of other simulations are shown in Supplementary Data Fig. A2.

The evolution of the leucosome mineralogy is shown from peak *T* to the water-saturated solidus. Melt loss could potentially occur at any temperature on the cooling path, in which case the preserved leucosome mineralogy would be that of the solids crystallized to that point. To illustrate this process, the leucosome mineralogy is recorded at the *T* step closest to 20, 50, and 80 wt % crystallization of the melt. Any free H_2O liberated during crystallization at the water-saturated solidus is assumed not to interact with the melanosome and to be completely lost (see White & Powell, 2010). The leucosome and melanosome mineralogical compositions are listed in Table 3, and the chemical compositions are recorded in Supplementary Data Table A3.

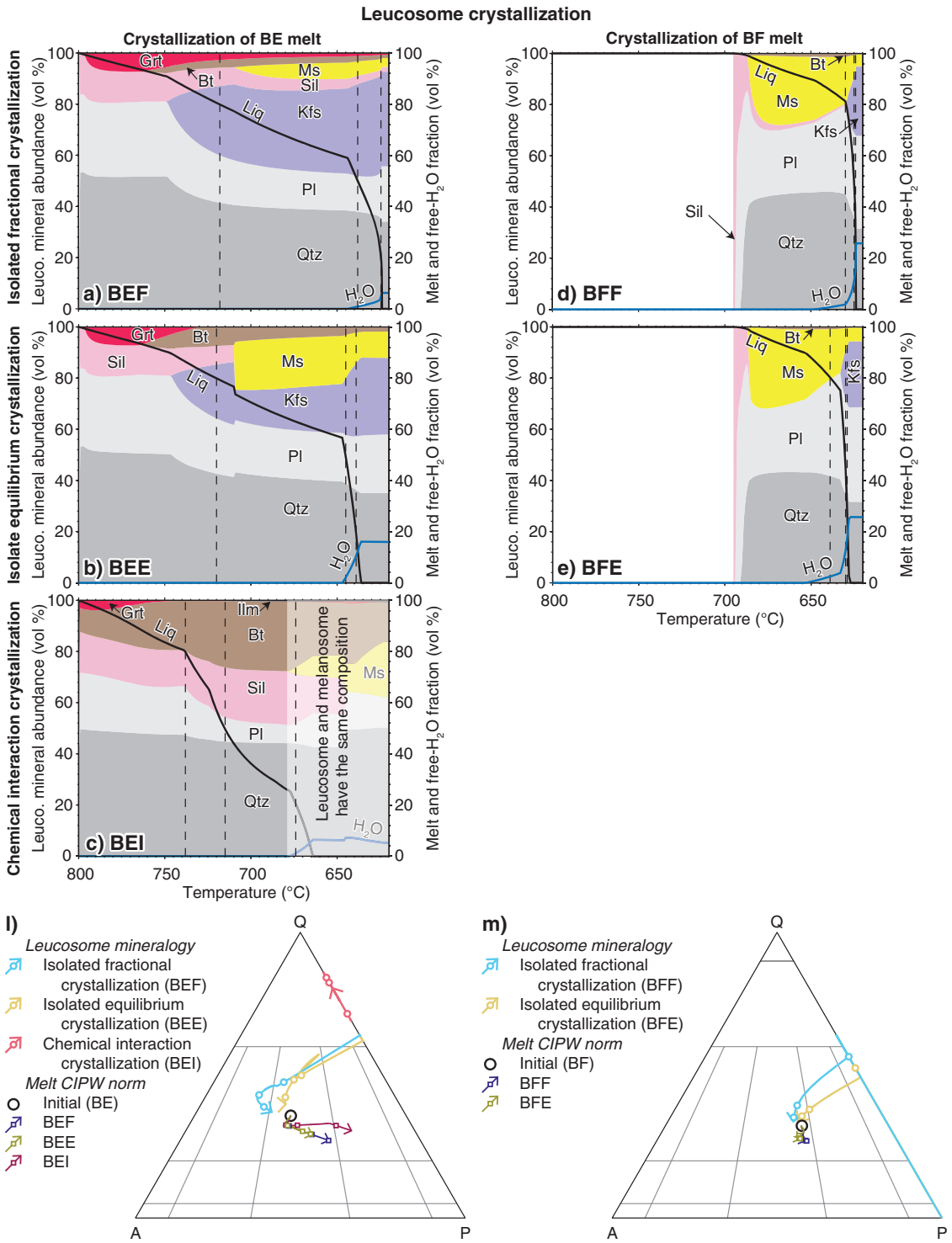

Fig. 6. (a–k) Evolving leucosome modal mineralogy, melt abundance, and free-H_2O abundance for different crystallization simulations as a function of decreasing *T*. (l–o) Quartz–alkali feldspar–plagioclase (QAP) ternary diagram of the leucosome mineralogy and the CIPW norm of the melt, with arrows pointing down-*T*. After about 80, 50, and 20 wt % crystallization of the melt, corresponding to the vertical dashed lines in (a)–(k), the composition of the leucosome is marked as a circle and the composition of the melt is marked as a square on the QAP diagram and is recorded in Table 3 and Supplementary Data Table A3.

Isolated fractional crystallization

IFC is simulated in a stepwise manner by decreasing *T* by 1°C, calculating the equilibrium composition, then subtracting the composition of the crystallized solid phases from the bulk composition, leaving a fractionated liquid. The volume of each mineral is incrementally summed after each step, giving the aggregate leucosome modal mineralogy as a function of *T* (Fig. 6a, d, f, i and l–o; Supplementary Data Fig. A2a, d, f and h–j).

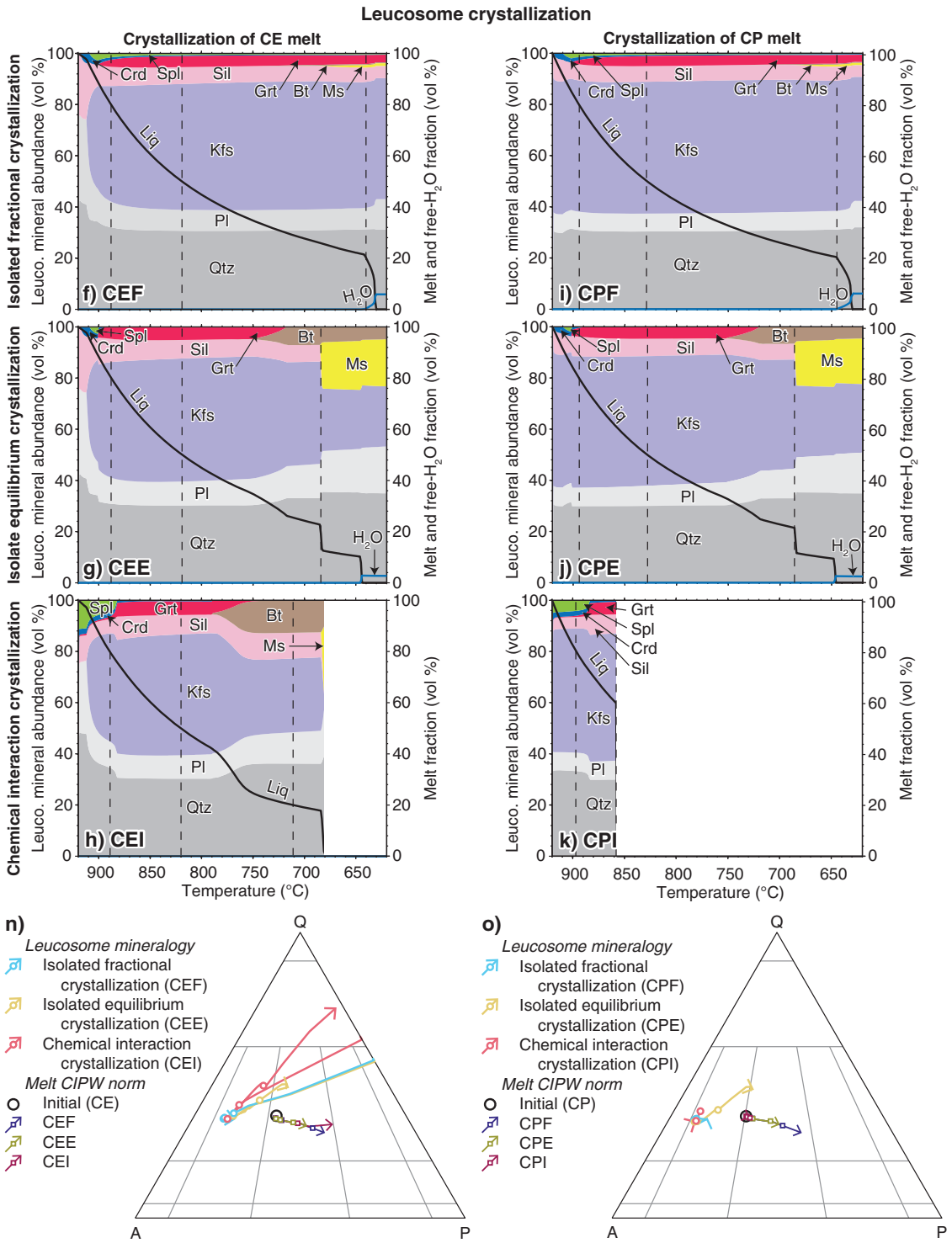

Fig. 6. Continued

Isolated equilibrium crystallization

IEC is simulated with a constant bulk composition, which is that of the peak-*T* melt. The leucosome composition is calculated every 1°C on the cooling path (modal mineralogy and leucosome compositions are plotted in Fig. 6b, e, g, j and l–o, and Supplementary Data Fig. A2, b, e, g and h–j).

Chemical interaction crystallization

During CIC, the melt and solids are physically segregated but maintain chemical communication as the melt crystallizes to form leucosome. After melt and solids segregate at peak *T*, chemical potential gradients develop between the melt-rich and the solid-rich domains during cooling that drive chemical diffusion

Table 3: Leucosome and melanosome compositions in all crystallization models after approximately 80, 50, and 20% melt crystallization

Model	MVR	T	Leucosome		Melanosome mineral assemblage (+ Qtz)
abbrev.	(vol.%)	(°C)	Igneous name	Minor phases	
AEF	80	749	Leucosyenogranite	Bt + Grt + Sil	Bt + Grt + Sil + Kfs + Pl + Ilm
	50	632	Leucosyenogranite	Bt + Grt + Sil + Ms	Bt + Grt + Sil + Kfs + Pl + Ilm
	18	624	Leucosyenogranite	Bt + Grt + Sil + Ms	Bt + Grt + Sil + Kfs + Pl + Ilm
AEE	80	750	Leucosyenogranite	Bt + Grt + Sil	Bt + Grt + Sil + Kfs + Pl + Ilm
	50	647	Leucomonzogranite	Bt + Ms	Bt + Grt + Sil + Kfs + Pl + Ilm
	23	632	Leucomonzogranite	Bt + Ms	Bt + Grt + Sil + Kfs + Pl + Ilm
AEI	80	763	Syenogranite	Bt + Grt + Sil + Ilm	Bt + Grt + Sil + Kfs + Pl + Ilm
	56	702	Monzogranite*	Bt + Sil + Ms + Ilm	Bt + Sil + Ms + Pl + Ilm
	20	666	Tonalite	Bt + Grt + Ms + Ilm	Bt + Grt + Sil + Ms + Pl + Ilm
AFF	80	691	Leucosyenogranite	Bt + Grt + Sil + Ms	Bt + Grt + Sil + Kfs + Pl + Ilm
	50	626	Leucosyenogranite	Bt + Grt + Sil + Ms	Bt + Grt + Sil + Kfs + Pl + Ilm
	25	624	Leucomonzogranite	Bt + Grt + Sil + Ms	Bt + Grt + Sil + Kfs + Pl + Ilm
AFE	80	694	Leucomonzogranite	Bt + Ms	Bt + Grt + Sil + Kfs + Pl + Ilm
	50	631	Leucomonzogranite	Bt + Ms	Bt + Grt + Sil + Kfs + Pl + Ilm
	20	629	Leucomonzogranite	Bt + Ms	Bt + Grt + Sil + Kfs + Pl + Ilm
BEF	80	718	Monzogranite*	Bt + Grt + Sil	Bt + Grt + Sil + Pl + Ilm
	50	638	Leucosyenogranite*	Bt + Grt + Sil + Ms	Bt + Grt + Sil + Pl + Ilm
	20	625	Leucosyenogranite*	Bt + Grt + Sil + Ms	Bt + Grt + Sil + Pl + Ilm
BEE	80	720	Monzogranite*	Bt + Sil	Bt + Grt + Sil + Pl + Ilm
	49	645	Leucomonzogranite*	Bt + Ms	Bt + Grt + Sil + Pl + Ilm
	19	639	Leucomonzogranite*	Bt + Ms	Bt + Grt + Sil + Pl + Ilm
BEI	80	738	Tonalite	Bt + Grt + Sil	Bt + Grt + Sil + Pl + Ilm
	50	715	Tonalite	Bt + Sil + Ilm	Bt + Grt + Sil + Pl + Ilm
	20	674	Tonalite	Bt + Grt + Sil + Ms + Ilm	Bt + Grt + Sil + Ms + Pl + Ilm
BFF	81	630	Trondhjemite	Bt + Sil + Ms	Bt + Grt + Sil + Kfs + Pl + Ilm
	50	625	Leucomonzogranite	Bt + Sil + Ms	Bt + Grt + Sil + Kfs + Pl + Ilm
	23	624	Leucomonzogranite	Bt + Sil + Ms	Bt + Grt + Sil + Kfs + Pl + Ilm
BFE	80	639	Trondhjemite	Bt + Ms	Bt + Grt + Sil + Kfs + Pl + Ilm
	45	630	Granodiorite	Bt + Ms	Bt + Grt + Sil + Kfs + Pl + Ilm
	27	629	Monzogranite	Bt + Ms	Bt + Grt + Sil + Kfs + Pl + Ilm
CEF	80	888	Syenogranite*	Crd + Grt + Hc + Sil	Crd + Grt + Hc + Sil + Pl + Ilm
	50	819	Syenogranite*	Crd + Grt + Hc + Sil	Crd + Grt + Hc + Sil + Pl + Ilm
	20	640	Leucosyenogranite*	Bt + Crd + Grt + Hc + Sil + Ms	Crd + Grt + Hc + Sil + Pl + Ilm
CEE	80	888	Leucosyenogranite*	Grt + Sil	Crd + Grt + Hc + Sil + Pl + Ilm
	50	819	Syenogranite*	Grt + Sil	Crd + Grt + Hc + Sil + Pl + Ilm
	19	684	Syenogranite*	Bt + Sil + Ms	Crd + Grt + Hc + Sil + Pl + Ilm
CEI	80	889	Syenogranite	Crd + Grt + Hc + Sil	Crd + Grt + Sil + Kfs + Pl + Ilm
	50	820	Syenogranite	Crd + Grt + Sil	Crd + Grt + Sil + Kfs + Pl + Ilm
	20	711	Syenogranite	Bt + Sil	Bt + Sil + Kfs + Pl + Ilm
CFF	80	726	Leucosyenogranite	Bt + Grt + Sil	Crd + Grt + Hc + Sil + Kfs + Pl + Ilm
	50	636	Leucosyenogranite	Bt + Grt + Sil + Ms	Crd + Grt + Hc + Sil + Kfs + Pl + Ilm
	9	631	Leucosyenogranite	Bt + Grt + Sil + Ms	Crd + Grt + Hc + Sil + Kfs + Pl + Ilm
CFE	80	727	Leucosyenogranite	Bt + Grt + Sil	Crd + Grt + Hc + Sil + Kfs + Pl + Ilm
	51	641	Leucomonzogranite	Bt + Ms	Crd + Grt + Hc + Sil + Kfs + Pl + Ilm
	24	638	Leucomonzogranite	Bt + Ms	Crd + Grt + Hc + Sil + Kfs + Pl + Ilm
CPF	80	894	Leucosyenogranite	Crd + Grt + Hc + Sil	Crd + Grt + Hc + Sil + Kfs + Pl + Ilm
	50	829	Syenogranite	Crd + Grt + Hc + Sil	Crd + Grt + Hc + Sil + Kfs + Pl + Ilm
	20	645	Leucosyenogranite	Bt + Crd + Grt + Hc + Sil + Ms	Crd + Grt + Hc + Sil + Kfs + Pl + Ilm
CPE	80	894	Leucosyenogranite	Crd + Grt + sil	Crd + Grt + Hc + Sil + Kfs + Pl + Ilm
	50	828	Leucosyenogranite	Grt + Sil	Crd + Grt + Hc + Sil + Kfs + Pl + Ilm
	21	686	Syenogranite	Bt + Sil	Crd + Grt + Hc + Sil + Kfs + Pl + Ilm
CPI	80	897	Syenogranite	Crd + Grt + Hc + Sil	Crd + Grt + Hc + Sil + Kfs + Pl + Ilm
	61	858	Leucosyenogranite	Crd + Grt + Sil	Crd + Grt + Sil + Kfs + Pl + Ilm

MVR, melt volume prior to the retrograde melt loss event.
*Model in which the leucosome contains K-feldspar, but the melanosome does not.

(White & Powell, 2010). A rigorous treatment of coupled melanosome and leucosome evolution requires calculation of chemical potentials and diffusion, a challenge that is beyond the scope of this study. Here, we develop a simplified model called chemical interaction crystallization that encompasses many of the important features.

At peak T, the system is segregated into two domains: domain m initially consists of all of the peak-T solids and has the composition $X_m = 0$; domain ℓ initially consists of all of the peak-T liquid and has the composition $X_\ell = 1$. During cooling and crystallization, domain m evolves to form the melanosome, and domain ℓ begins as only melt, then evolves to melt plus minerals crystallized from the melt, and finally to the solid minerals that constitute the leucosome. Two key approximations are made that dictate the crystallization during cooling. First, diffusion between the two

domains is assumed to move their compositions towards one another in a straight line through composition space. Second, chemical potential differences, and therefore mass transfers, are approximated to be zero if both domains have the same mineral assemblage, even if the compositions of the minerals in each domain are different (in practice, the differences tend to be small).

The first approximation simplifies diffusion to a single compositional parameter, *X*. The parameter *X* is a linear multi-component compositional scale where zero is the composition of the residuum at peak *T* and unity is the composition of the melt at peak *T*; consequently, $X = 0{\cdot}5$ corresponds to a composition of half of the residuum and half of the melt at peak *T*, which is the same as the composition of all solids and melt on the prograde path, after all prograde melt loss. Diffusion changes the composition of each domain simultaneously during cooling: the compositions of the two domains move towards one another such that X_m increases as X_ℓ decreases. The compositional evolution of the melanosome and leucosome is illustrated in *T*–*X* phase diagrams in Fig. 5 and Supplementary Data Fig. A1.

The second approximation relaxes the definition of equilibrium. With each -1°C increment of cooling, the physically segregated domains undergo independent and different reactions, forming different mineral assemblages. Because chemical potential gradients must exist between two domains with different assemblages, mass transfer between the two domains is then assumed to occur as a result of diffusion (as approximated with the first assumption): the compositions of the two domains move towards one another until they both have the same mineral assemblage (albeit with different mineral proportions), at which point the chemical potential gradients are assumed to be eliminated and diffusion ceases. This model can be implemented by starting with $X_m = 0$ and $X_\ell = 1$ at peak *T* on a *T*–*X* diagram, then tracing mineral assemblage boundaries inwards while moving down-*T* such that both the leucosome and melanosome compositions plot on either side of the same assemblage field (arrows in Fig. 5 and Supplementary Data Fig. A1).

Leucosome mineralogy and chemical composition

The simulated mineralogical and chemical compositions of the leucosome vary widely in the different simulations, ranging from tonalite to syenogranite (Table 3; Fig. 6; Supplementary Data Fig. A2). In addition to the Qtz and feldspars that dominate the mode, there are also differences in minor minerals. These variations are dictated by the initial melt composition, the crystallization process, and the extent and temperature of retrograde melt loss.

Effect of initial melt composition

The initial melt composition is the primary determinant of leucosome mineralogy, in particular the QAP ratio. For example, tonalite–trondhjemite to monzogranite leucosomes with the largest Pl:Kfs ratios crystallized from melt BF (Fig. 6m), the melt with the most normative Pl of the simulated melts, whereas syenogranite leucosomes with the greatest Kfs:Pl ratios crystallized from melt CP (Fig. 6o), the melt with the most normative Kfs.

Effect of isolated fractional, isolated equilibrium, and chemical interaction crystallization

The crystallization process influences the QAP ratios of the leucosome to some degree, but has its major effect on the minor minerals. Within a limited range of QAP ratios, leucosomes from IFC simulations tend to plot closer to the Q–A join, whereas leucosomes from IEC simulations plot closer to the Q–P join (Fig. 6l–o). For example, starting with melt BE, BEF produces monzogranite to syenogranite leucosome, whereas BEE produces more Pl-rich monzogranite leucosome (Fig. 6l). Leucosomes from the CIC simulations typically plot between the leucosomes of the IEC and IFC simulations, with an intermediate Kfs:Pl ratio. An exception is simulation BEI, in which tonalite leucosome is produced for all temperatures (Fig. 6c) because chemical interaction with the melanosome suppresses crystallization of Kfs in favour of Bt.

IEC and CIC simulations produce a greater volume of the hydrous phases Bt and Ms than their IFC counterparts. In IFC simulations, minor minerals crystallize directly from the melt, whereas in IEC simulations, previously crystallized minerals in the leucosome are involved in later reactions. In CIC simulations, minerals in both the leucosome and melanosome react with the melt. For example, Bt forms at the expense of Grt by the reverse of reactions such as reactions 8–10 and 12–14 in several of the IEC and CIC simulations (e.g. Fig. 6b and c), whereas Ms forms at the expense of Sil and Kfs by the reverse of reaction 4 (e.g. Fig. 6b). The retrograde reactions predicted in the simulations may, in natural migmatites, reveal themselves as replacement textures indicative of these reactions and processes. A consequence of the chemical interactions in the CIC simulations is that leucosomes commonly have a relatively high proportion of mafic minerals, more than is typical of many natural pelitic leucosomes, which have less than 10 vol. % mafic minerals.

Effect of retrograde melt loss

Leucosome mineralogy evolves as *T* decreases so that the timing of retrograde melt loss affects the resulting leucosome. Typically, the temperature of melt loss has a relatively small effect on the QAP ratio of the leucosome (Table 3). For example, IFC of melt CE produced a syenogranite leucosome regardless of whether melt was lost at 888°C or 640°C (Fig. 6f). In only three of the simulations, the timing of melt loss has a significant effect on the leucosome type, between tonalite–trondhjemite and granite. Simulation BFF predicts a

trondhjemite leucosome after 19 wt % crystallization, and a monzogranite leucosome after either 50 or 77 wt % crystallization, because the crystallization of Kfs begins after about 20 wt % crystallization (Fig. 6d). Simulation AEI predicts syenogranite leucosome after 20 wt % crystallization and tonalite leucosome after 80 wt % crystallization because Kfs is completely consumed by a Ms-producing retrograde reaction after about 38 wt % crystallization (Supplementary Data Fig. A2c).

Minor minerals change markedly with decreasing *T*. Anhydrous minerals, including Sil ± Grt ± Spl ± Crd, crystallize at higher *T* whereas hydrous minerals, Bt followed by Ms, crystallize at lower *T*. This suggests that minor minerals may be useful for constraining the temperature of retrograde melt loss if they can be identified as products from melt-crystallization reactions. For example, in simulation CEI, Bt first appears in the leucosome at 790°C. If a natural rock followed this simulation, a Bt-absent leucosome would indicate that all melt was lost, and crystallization ceased, above 790°C.

Melt composition extracted during retrograde melt loss

As the leucosome crystallizes, the composition of the melt changes. The CIPW norm of the evolving melt composition is shown on the QAP triangles in Fig. 6l–o and Supplementary Data Fig. A2h–j; the chemical composition of the melt at different retrograde melt loss events is recorded in Supplementary Data Table A4 and shown as squares in the QAP triangles. As *T* decreases, the melt composition tends to increase in normative Pl relative to Afs, decrease slightly in normative Qtz, and become more hydrous for most models; only if trondhjemite–tonalite leucosome crystallizes following excess-water melting do melt compositions increase in normative Afs (Fig. 6l and m). The melt composition changes the most during crystallization in the CIC simulations, and the least during IEC; however, the compositional changes of the melt are relatively small in all simulations. All melts extracted during retrograde melt loss are normative monzogranite, except for the normative granodiorite melt extracted during the lowest-*T* melt loss events for simulations BEI (Fig. 6l) and AEI (Supplementary Data Fig. A2h).

Plagioclase composition

Plagioclase is potentially a sensitive indicator of solidification processes in migmatites (Fourcade *et al.*, 1992; Nabelek, 1999; Kriegsman, 2001). In the IEC and IFC simulations, the melanosome does not react with the melt on cooling. The melanosome Pl therefore does not change in composition from peak conditions, whereas the Pl in the leucosome becomes increasingly sodic (Fig. 7; Supplementary Data Fig. A3). For example, during simulation AEF, the mole fraction of anorthite (X_{An}) in melanosome Pl is 0·31 regardless of *T*. Leucosome Pl

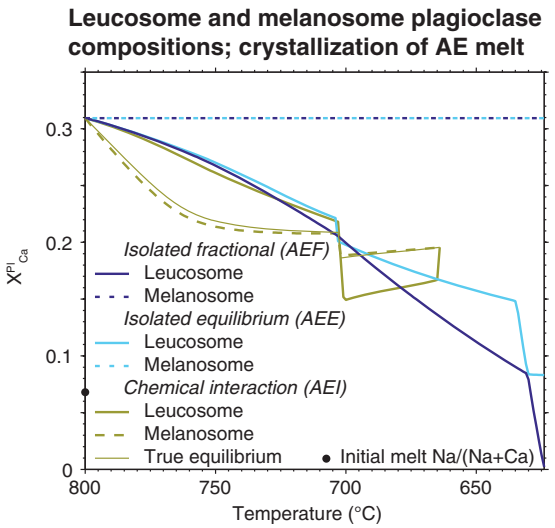

Fig. 7. Instantaneous plagioclase composition (X^{Pl}_{Ca}) as a function of decreasing *T* for the three crystallization simulations that involve melt AE (IFC, AEF; IEC, AEE; CIC, AEI) and the composition of plagioclase during the AE melting simulation, which shows the melanosome and leucosome plagioclase composition if crystallization occurred via true equilibrium crystallization.

composition, in contrast, first crystallizes with the composition $X_{An} = 0{\cdot}31$ at 799°C and becomes more sodic as *T* decreases, such that the final (albeit modally minor) increment of Pl crystallization has the composition $X_{An} = 0{\cdot}00$ at 624°C. In natural migmatites, IFC may be expected to result in normally zoned leucosome Pl, whereas unzoned leucosome Pl is expected from IEC, even though the instantaneous Pl composition becomes progressively more sodic as the melt crystallizes.

In contrast, leucosome and melanosome Pl compositions are similar in the CIC simulations. In simulation AEI, for example, both leucosome and melanosome Pl become increasingly sodic to 702°C, and then they both become more calcic at lower *T* (Fig. 7). The absolute difference in X_{An} between leucosome and melanosome Pl is relatively small, 0·00–0·05, with a mean of 0·03. Because of the approximations in the chemical interaction model, leucosome and melanosome Pl compositions are not identical, as would be the case during true equilibrium crystallization in which the melanosome and leucosome are in complete chemical communication.

Solidification temperature

A partially molten rock may make the transition into a completely solid migmatite by either the crystallization of the last remaining melt at the solidus or the physical loss of all melt at some point between peak *P*–*T* conditions and the solidus. A combination of the crystallization process and the temperature of possible melt loss during prograde melting or retrograde crystallization determines the temperature of this transition, herein called the solidification temperature. The solidification temperature is of importance to rheological studies

because it is the minimum T at which a partially molten rock, weakened by the presence of melt, becomes solid and strong during crystallization (Vigneresse *et al.*, 1996; Rosenberg & Handy, 2005).

If there has been neither prograde nor retrograde melt loss from a pelitic protolith that was not previously melted, final solidification occurs at the water-saturated solidus, the temperature of which depends on the bulk composition. The IEC and IFC simulations crystallize to the granitoid melt solidus (624–643°C at the 6·5 and 5·3 kbar pressures considered here). The CIC simulations that lost no melt crystallize progressively until the water-saturated solidus of the pelitic source composition ($X = 0{\cdot}5$) is reached (660–664°C at 6·5 and 5·3 kbar). As the water-saturated solidus is reached, the second approximation of the CIC model demands that both domains have the same phases, including melt and free H_2O. Although unrealistic, this causes the two domains to exchange components through simulated diffusion at the temperature of the water-saturated solidus until they have the same compositions.

Prograde melt loss is commonly cited as a means to increase the solidification temperature (e.g. White & Powell, 2002). This interpretation implies equilibration between leucosome and melanosome during crystallization and was approximated in this study with the CIC simulation CPI. In this simulation, the system solidifies at 857°C, ~200°C above the water-saturated solidus (Fig. 6k). In contrast, the solidification temperature during IEC and IFC simulations is insensitive to prograde melt loss. After prograde melt loss in simulation CP, solidification occurs at 630°C in the IFC simulation (CPF; Fig. 6i), and at 646°C in the IEC simulation (CPE; Fig. 6j). In these examples, as well as all other IEC and IFC simulations, crystallization continues to a water-saturated solidus and free H_2O is released. The liberated H_2O has the potential to drive retrograde hydration reactions in the melanosome, or partially melt nearby rocks with lower wet solidus temperatures, and thereby leave petrographic evidence.

Summary of crystallization simulation results

Our simulations produce a diversity of simulated migmatites by varying five factors: initial melt composition; isolated melt crystallization vs crystallization of melt in chemical communication with the melanosome; IFC vs IEC; prograde melt loss; retrograde melt loss. For the simulated pelitic protolith compositions, leucosome compositions range from syenogranite to tonalite–trondhjemite, with the majority being granite. The initial melt composition is the most influential factor that dictates the igneous rock name of the leucosome. The timing of retrograde melt loss is also important in some examples: in some simulations high-T melt loss preserves tonalite–trondhjemite leucosome, whereas lower-T melt loss preserves granite; in other simulations, Kfs is replaced by Ms at intermediate T, so high-T melt loss preserves granite, whereas low-T melt loss preserves tonalite–trondhjemite.

The CIPW normative composition of melt lost during cooling is typically monzogranite or rarely granodiorite. At high T, the melt lost during retrograde melt loss events is similar to the initial melt composition, but as crystallization continues, the melt composition is increasingly dictated by the melt loss temperature and crystallization process. The melts with the most normative Pl crystallize at low T from CIC simulations and, to a lesser extent, IFC simulations.

Plagioclase compositions in leucosomes and melanosomes are predicted to be indicative of different crystallization processes. Leucosome Pl that is more sodic than melanosome Pl is suggestive of crystallization of melt in chemical isolation from the melanosome, whereas Pl with similar compositions in the leucosome and melanosome implies chemical interaction between the two during crystallization. Normally zoned Pl is indicative of IFC.

The solidification temperature of all simulations is that of the bulk composition-dependent water-saturated solidus (624–664°C), unless modified by melt loss. Prograde melt loss can increase the solidification temperature by potentially hundreds of degrees Celsius but only if crystallization occurs via CIC. Retrograde melt loss may change the solidification temperature to anything between the peak T and the temperature of the water-saturated solidus.

APPLICATION TO NATURAL MIGMATITES

Limitations of the modelling

The modelling carried out in this study makes a number of simplifications regarding our knowledge of nature. The chemical subsystem considered in the thermodynamic modelling omits several system components that occur in natural pelitic rocks that may influence phase relations. In nature, the presence of CO_2 (e.g. Connolly & Cesare, 1993; Bartoli *et al.*, 2013) and saline solutions (e.g. Misiti *et al.*, 2005; Touret & Huizenga, 2011) have the potential to reduce the activity of water and consequently the amount of melt. Including Fe^{3+} in the modelling would affect the mineral assemblages and stabilities in the phase diagrams (Boger *et al.*, 2012), mainly because Fe^{3+} influences the stability of oxide phases (especially Ilm, Mag, and Spl), and it increases the stability of Bt, Grt and, to a lesser degree, Ms, into which Fe^{3+} partitions (White *et al.*, 2000). Including boron in the modelling would lower the solidus temperature (Chorlton & Martin, 1978; Benard *et al.*, 1985) and potentially stabilize tourmaline, which is common in pelitic rocks and leucogranites. Fluorine increases the stability of Bt (Pattison, 1987; Peterson *et al.*, 1991; Nair & Chacko, 2002) and lowers the solidus temperature (Wyllie & Tuttle, 1961). Zinc increases the stability of Spl and staurolite (Ashworth, 1975; Nichols *et al.*, 1992).

Temperatures in our modelling study are reported exactly, without any uncertainty estimate; however, numerical uncertainties must be taken into account when applying the results from this study to actual rocks. Uncertainties in empirically determined parameters in the thermodynamic end-member dataset propagate to uncertainties in the position of phase diagram boundaries of the order of tens of degrees Celsius (Powell & Holland, 1988). Including uncertainties in the activity–composition parameters, which are reported only in some studies, probably increases uncertainties in phase diagram calculations by at least a factor of two (Powell & Holland, 2008). Uncertainty in the measurement of the bulk composition introduces of the order of 1–10°C of uncertainty in the position of phase boundaries (Palin *et al.*, 2016). The total uncertainties in T are probably of the order of several tens of degrees Celsius.

Several processes that are thought to be involved in the formation of some migmatites were not modelled here. During melt segregation, residuum material and peritectic phases may be entrained into the melt-dominated domains (Stevens *et al.*, 2007; Villaros *et al.*, 2009; Taylor *et al.*, 2010; Sawyer, 2014), making the leucosome composition not simply the solids that crystallized from a melt, as modelled here. Several experimental studies have found that equilibrium with Pl is not attained during melting experiments at $T < 800$°C; instead, Pl dissolves stoichiometrically with little or no change in Pl composition (Johannes, 1978, 1980, 1984; Acosta-Vigil *et al.*, 2006). If Pl does not equilibrate during the time scale of melting reactions and melt extraction in nature, the melt and leucosome major element compositions would be different from what is modelled here.

Our modelling did not consider how melt is physically squeezed out of the residuum (segregation) or how melt is forced away from the site of melting (melt loss). The degree of melt extraction is probably dictated by the structural evolution of the partially molten system (e.g. Rosenberg & Handy, 2001; Rutter & Mecklenburgh, 2006). The presence of pseudomorphs after melt-filled pores suggests that melt is only partially extracted from the residuum [e.g. 4·2–25·1 vol. % pseudomorphs were reported by Holness & Sawyer (2008)]. The degree of separation of the melt and residuum will particularly affect the melt and residuum compositions, the melt volume, and the extent of retrograde reactions.

Leucosome compositions

The leucosome in pelitic migmatites varies from tonalite–trondhjemite to alkali feldspar granite (e.g. Powell & Downes, 1990; Vernon *et al.*, 2001; Sawyer, 2008*a*), similar to the range observed in our simulations. The range in composition in natural migmatites therefore implies a variety of melting and crystallization processes. Granite was the most common leucosome composition predicted in our simulations (Table 3), suggesting that it is relatively ineffective as a discriminant of different processes. On the other hand, non-granitic leucosomes are indicative of more specific melting and crystallization processes.

Tonalite–trondhjemite leucosome has been observed in several metapelitic migmatites (Sawyer, 1987; Whitney & Irving, 1994; Solar & Brown, 2001; Cruciani *et al.*, 2008; Hamilton *et al.*, 2012). Tonalite–trondhjemite leucosome formation has been interpreted to require either an influx of water during melting (Whitney & Irving, 1994) or the accumulation of early crystallized Qtz and Pl followed by the loss of K-rich melt owing to fractional crystallization (Sawyer, 1987; Solar & Brown, 2001; Cruciani *et al.*, 2008; Morfin *et al.*, 2014). Our simulations suggest two means of crystallizing tonalite–trondhjemite leucosome. The first involves crystallization of tonalite–trondhjemite from excess-water melt, as inferred in the above studies. A second mechanism, for melts generated by dehydration melting, is the back-reaction and complete replacement of Kfs by Ms through the reverse of reaction 4. One mechanism that does not appear to be viable to form tonalite–trondhjemite leucosome is partial fractional crystallization of a melt produced from dehydration melting, followed by melt loss, because all leucosomes simulated here by this process are granitic (Table 3). We note that these conclusions pertain to a pelitic bulk composition; K-poor greywacke and intermediate and mafic migmatites, for example, commonly have tonalite–trondhjemite leucosomes.

Alkali feldspar granitic leucosome observed in nature (Powell & Downes, 1990; Vernon *et al.*, 2001) has been hypothesized to be a cumulate of early crystallized minerals (Ellis & Obata, 1992). In our simulations, Kfs and Qtz never crystallized together without Pl, arguing against the cumulate hypothesis [Scaillet *et al.* (1995) found similar results in their experimental studies]. An alternative hypothesis is preferential growth of peritectic Kfs in melt-rich domains (Powell & Downes, 1990), but our simulations did not test this possibility.

Although granitic leucosome on its own puts few constraints on melting or crystallization processes, granite leucosome associated with a Kfs-absent melanosome, such as reported by Hamilton *et al.* (2012), is a special case. Our simulations suggest that this situation may arise either if Kfs is completely consumed into the melt phase on the prograde path (e.g. Fig. 3j) or if Kfs in the melanosome participates in retrograde reactions and is consumed during cooling (e.g. Supplementary Data Fig. A1f).

Relationships between leucosome, melt, and granite geochemistry

Geochemical studies consider the compositional links between peraluminous leucogranite, leucosome in migmatites and melts. The compositions of leucosome in migmatites have been compared with leucogranites to test possible relationships between granitic suites and source areas or protoliths (Obata *et al.*, 1994; Castro *et al.*, 1999; Jung *et al.*, 2000; Otamendi & Patiño Douce,

2001; Johannes *et al.*, 2003; Burda & Gawęda, 2009), and with experimentally produced and thermodynamically calculated melts to understand the formation of leucosomes (Solar & Brown, 2001; Cruciani *et al.*, 2008; Taylor *et al.*, 2014). Similarly, the compositions of leucogranites are compared with experimental and thermodynamically calculated melts to understand the source of the melt and the genesis of the granites (e.g. Patiño Douce & Harris, 1998; Pressley & Brown, 1999; Dini *et al.*, 2005; Stevens *et al.*, 2007). Although melts, leucosomes, and leucogranites are related, they each form in a different manner, and are imparted with slightly different compositions.

Previous studies found that leucosome compositions are more diverse than the composition of experimental melts (Sawyer, 1987; Nabelek *et al.* 1992; Harris *et al.*, 2004; Sawyer, 2008*a*). Similarly, our modelling study found that simulated leucosome compositions span a wider range in composition than the melts from which they were derived (Figs 4 and 6). Melt loss during crystallization yields dry leucosomes that in some cases are Pl accumulations. Any chemical interactions of melt, leucosome, and melanosome during crystallization move leucosome compositions away from experimental or peak-*T* melt compositions.

Leucosome chemical compositions need not be the same as the compositions of related leucogranites. Even if a leucosome and a leucogranite began with the same melt composition and crystallized along the same *P–T* path to the solidus, the resulting leucosome and leucogranite could end up with different compositions and mineralogies if the melanosome interacted with the melt and leucosome during crystallization. However, because of prograde or retrograde melt loss, the composition of the crystallized, solid leucosome may be different from that of the melt lost from the partially molten rock (Figs 4 and 6), the latter of which has the potential to collect and form leucogranites (Sawyer, 2008*b*). Also, the *T* interval of crystallization may be different for leucosomes and leucogranites. Whereas leucosomes commonly contain minor phases such as Grt and Crd, believed to indicate crystallization at relatively high *T* (Powell, 1983; Waters, 1988; Powell & Downes, 1990; Carson *et al.*, 1997; White *et al.*, 2001; White & Powell, 2002; Guernina & Sawyer, 2003; Ward *et al.*, 2008; Morfin *et al.*, 2014), leucogranite commonly contains micas (e.g. Frost *et al.*, 2001), suggesting crystallization to or near the water-saturated solidus. If the leucosome represents high-*T* crystallization and leucogranites represent the lower-*T* crystallization of the melt lost from the partially molten region (e.g. Sawyer, 1987), they probably have some chemical compositional differences.

Unlike leucosomes, leucogranites may have major element compositions similar to the melts from which they were derived, with the exception of H_2O and other volatile elements (e.g. Patiño Douce & Harris, 1998). For this reason, the compositions of melts extracted from crustal protoliths are of interest to granite geochemists, who try to relate trends in granite composition to the melt composition, and ultimately the protolith (e.g. Solar & Brown, 2001; Wang *et al.*, 2011). Also of interest should be the nature of melting processes in the source region (Fig. 6l–o; Supplementary Data Fig. A2h–j). Although the protolith composition plays the largest role, the melting temperature and the availability of water in the source area also affect the major element melt composition, including the amount of water in the melt (Fig. 4; Vielzeuf & Holloway, 1988; Patiño Douce & Harris, 1998). Melt composition is additionally varied by the extent of chemical interaction of the melt with the residuum, and the crystallization processes that precede or accompany melt loss (Figs 4 and 6l–o; Supplementary Data Tables A2 and A4 and Fig. A2i–j).

THE EFFECT OF HETEROGENEITY ON TEMPERATURE ESTIMATION OF PELITIC MIGMATITES

Up to this point, the discussion has been concerned with forward modelling of different melting and crystallization processes. For petrologists studying migmatites in the field, however, the problem is to understand the formation of these complex rocks, which are the end point of a variegated series of processes that are not known in advance. In this section, we use the simulated migmatites to address two common questions in the analysis of natural migmatites. (1) Is it possible to constrain the *P–T* evolution of migmatites that underwent open-system processes? (2) Should only the melanosome be sampled to estimate this *P–T* evolution, only the leucosome, or a combination of the two? Given that physically separating the leucosome and melanosome may be difficult in practice (Fig. 1), does it matter?

We address these questions by focusing on two salient *P–T* points, the peak *T* and the solidification temperature; the latter is of interest because of its relationship to rheology. We treat the simulated migmatites from the work described above (e.g. Fig. 5) as if they were migmatites encountered in the field, with a heterogeneous appearance typical of natural migmatites (Fig. 1). We concede that the migmatites may have lost melt, so the protolith composition cannot be directly measured from the rock. For each simulated migmatite, we estimate the peak and solidification temperatures from phase diagrams calculated for a bulk composition containing various melanosome:leucosome ratios. In our analysis, we focus on mineral assemblage fields rather than on mineral composition isopleths, because of the likelihood of down-*T* re-equilibration from peak conditions (Frost & Chacko, 1989; Fitzsimons & Harley, 1994; Pattison & Bégin, 1994). Consequently, the precision of the *T* estimates depends on the *P–T* extent of the mineral assemblage fields. For the high-variance assemblages commonly found in metagranites, metabasites, and some metagreywackes, mineral composition isopleths may be considered to increase the precision.

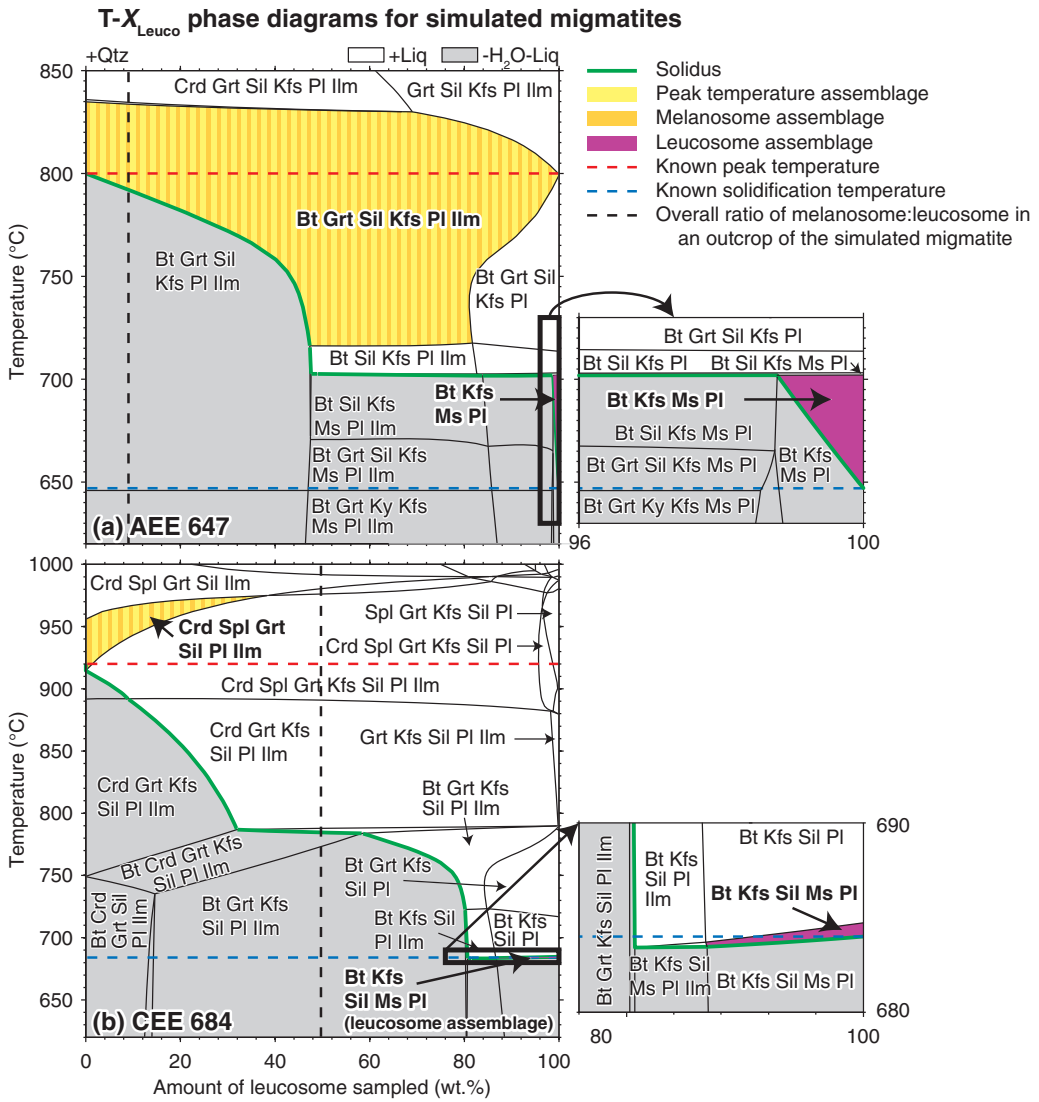

Fig. 8. Phase diagrams of temperature versus the amount of leucosome in the bulk composition (X_{Leuco}). The three-letter and three-digit label in each panel identifies the crystallization simulation (see text for further details). The raw data used in the construction of the diagrams are listed in Table 3 and Supplementary Data Table A3. Three mineral assemblage fields are highlighted in colour and by bold-face labels: the peak-temperature assemblage, which may not be preserved in the rock, but needs to be inferred using petrographic observations, and the mineral assemblages preserved in the melanosome and leucosome after solidification. Each thick green line highlights a solidus. The known peak and solidification temperatures, derived from the simulations, are shown with red and blue dashed lines, respectively.

Phase diagrams of *T* versus amount of leucosome sampled

The peak *P*–*T* conditions of a metamorphic rock are commonly estimated using a *P*–*T* phase diagram calculated for a single bulk composition sampled from an outcrop; the peak conditions are estimated to be the *P* and *T* ranges spanned by the inferred peak-*T* mineral assemblage field. Our aim is to understand how *T* estimates derived from phase diagrams change depending on whether the sample collected from outcrop consists of only melanosome, only leucosome, or a mixture of the two. Instead of calculating many *P*–*T* diagrams that correspond to different melanosome:leucosome ratios, we consider all possible combinations of melanosome and leucosome together by calculating isobaric phase diagrams of *T* versus amount of leucosome in the sampled migmatite bulk composition (*T*–X_{Leuco} phase diagrams) for each of the simulated migmatites (Fig. 8). In these diagrams, X_{Leuco} is the mass proportion of leucosome in the selected bulk composition, ranging from melanosome-only at $X_{Leuco} = 0$ to leucosome-only at $X_{Leuco} = 1$. Each phase diagram is referred to by three letters, corresponding to the crystallization simulation from the previous section, followed by a three-digit number, corresponding to the temperature of retrograde melt loss (e.g. phase diagram AEE 750 corresponds to the simulated migmatite formed in IEC simulation AEE that solidified during retrograde melt loss at 750°C). A vertical dashed line on each *T*–X_{Leuco} phase diagram indicates the amount of melanosome

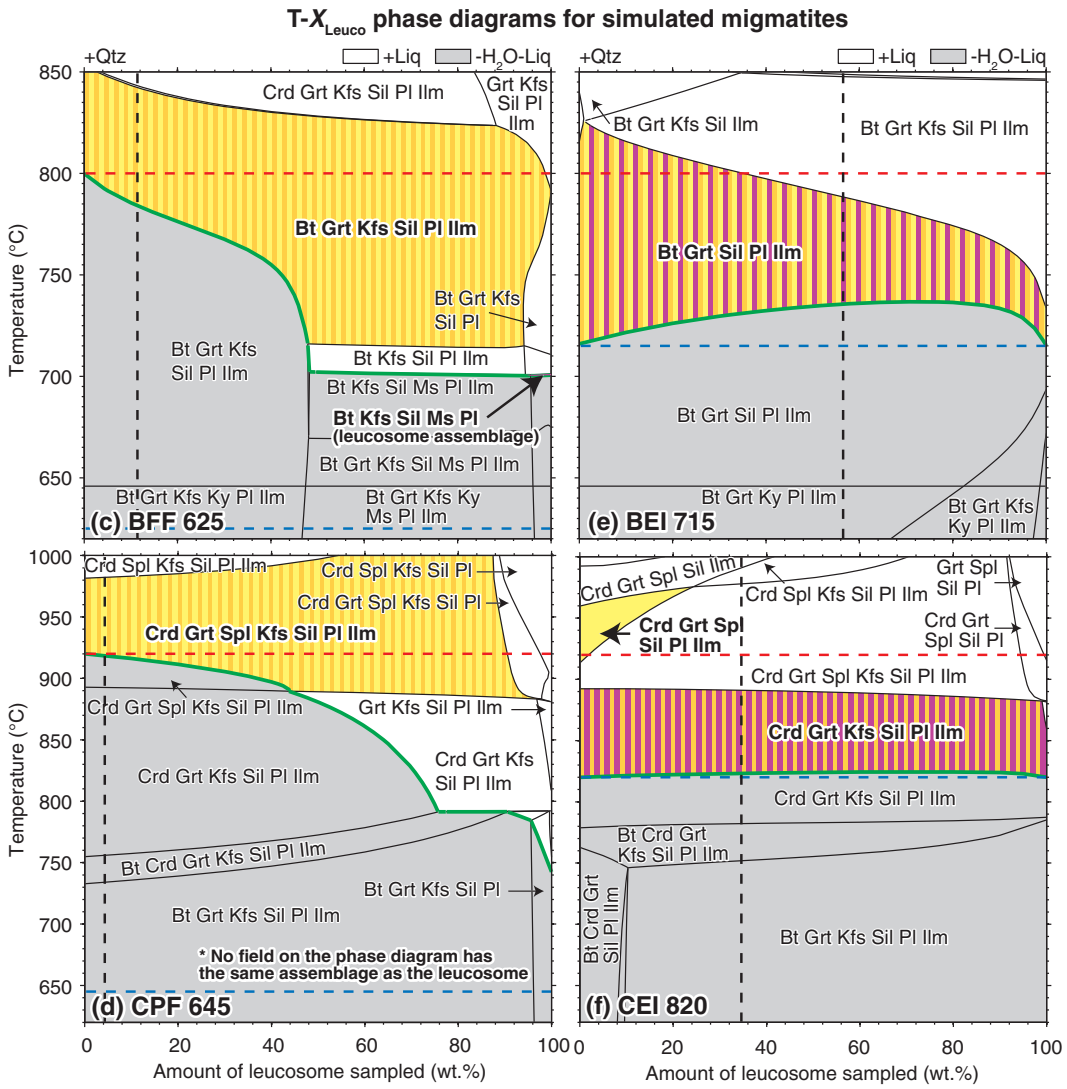

Fig. 8. Continued

and leucosome produced in the crystallization simulation. Because of retrograde and/or prograde melt loss, neither this vertical line nor any other value of X_{Leuco} can be assumed to correspond to the composition of the original source; this composition is no longer directly available from the outcrop. The known peak and solidification temperatures (those assumed in the simulations) are drawn as horizontal dashed lines in the phase diagrams. T–X_{Leuco} phase diagrams for the 32 simulated migmatites listed in Table 4 are shown in Supplementary Data Fig. A4 and a subset showing the main results is provided in Fig. 8.

Three mineral assemblage fields are highlighted in the T–X_{Leuco} phase diagrams: the melanosome, leucosome, and peak-T mineral assemblage fields. The melanosome and leucosome mineral assemblages are the mineral assemblages preserved in the (simulated) melanosome and leucosome, respectively, plus melt that is assumed to have been present just above the solidus. These two mineral assemblages can be determined from observations of the outcrop, or in our case, from the results of the simulations (Table 3; Figs 5 and 6; Supplementary Data Figs A1 and A2). The peak-T assemblage is the mineral assemblage and melt that was stable at peak T in the simulation. Because we simulated the migmatites, we know the peak-T assemblage, *a priori*, even if retrograde reactions consumed peak-T minerals and produced new lower-grade minerals. The petrologist studying the (simulated) outcrop must infer the peak-T assemblage, and we assume that they can make the correct inference petrographically using textural evidence such as mineral inclusion relationships, pseudomorphs and reaction textures. If retrograde melt loss took place, the bulk composition of the suprasolidus system at peak T is no longer retrievable from any combination of the melanosome and leucosome. Consequently, the T–X_{Leuco} diagram does not necessarily contain any field with the peak-T mineral assemblage.

The T–X_{Leuco} diagrams are used for three purposes. First, they are used to determine the optimal strategy

Table 4: Peak-temperature estimates (in °C) for melanosome bulk-compositions with various amounts of leucosome contamination

Sim. mig. abbrev.	Peak *T* Kfs	Amount of leucosome contamination (wt %)										
		0·0		10·0		20·0		30·0		Amount in simulated migmatite		
		$T^{Peak}_{Estimate}$	ΔT^{Peak}	$T^{Peak}_{Estimate}$	ΔT^{Peak}	$T^{Peak}_{Estimate}$	ΔT^{Peak}	$T^{Peak}_{Estimate}$	ΔT^{Peak}	X_{Leuco} (wt %)	$T^{Peak}_{Estimate}$	ΔT^{Peak}
AEE 750	Y	800·0	0·0	799·8	−0·2	799·5	−0·5	799·2	−0·8	3·9	799·9	−0·1
AEE 647	Y	800·0	0·0	791·1	−8·9	782·1	−17·9	772·1	−27·9	9·0	792·0	−8·0
AEE 632	Y	800·0	0·0	792·2	−7·8	784·4	−15·6	775·9	−24·1	12·1	790·6	−9·4
BEE 720	N	800·0	0·0	DNP		DNP		DNP		16·3	DNP	
BEE 645	N	800·0	0·0	DNP		DNP		DNP		31·2	DNP	
BEE 639	N	800·0	0·0	DNP		DNP		DNP		39·3	DNP	
CEE 888	N	920·0	0·0	955·0	35·0	DNP		DNP		20·8	DNP	
CEE 819	N	920·0	0·0	957·7	37·7	DNP		DNP		39·0	DNP	
CEE 684	N	920·0	0·0	943·0	23·0	958·9	38·9	969·0	49·0	49·7	DNP	
AFF 691	Y	800·0	0·0	795·5	−4·5	791·2	−8·8	786·4	−13·6	2·9	798·3	−1·7
AFF 626	Y	800·0	0·0	794·1	−5·9	788·5	−11·5	782·5	−17·5	6·3	796·1	−3·9
AFF 624	Y	800·0	0·0	794·2	−5·8	789·1	−10·9	783·7	−16·3	8·2	795·1	−4·9
BFF 630	Y	800·0	0·0	783·9	−16·1	771·1	−28·9	750·1	−49·9	6·4	789·0	
BFF 625	Y	800·0	0·0	785·5	−14·5	776·3	−23·7	767·6	−32·4	11·4	784·2	
BFF 624	Y	800·0	0·0	785·6	−14·4	777·6	−22·4	770·9	−29·1	16·7	778·0	
CFF 726	Y	920·0	0·0	916·0	−4·0	911·4	−8·6	905·6	−14·4	5·2	918·0	−2·0
CFF 636	Y	920·0	0·0	901·5	−18·5	890·0	−30·0	889·4	−30·6	11·1	898·9	−21·1
CFF 631	Y	920·0	0·0	904·2	−15·8	889·5	−30·5	888·7	−31·3	14·0	896·3	−23·7
CPF 894	Y	920·0	0·0	919·6	−0·4	919·5	−0·5	919·3	−0·7	1·2	919·8	
CPF 829	Y	920·0	0·0	919·7	−0·3	919·3	−0·7	918·8	−1·2	2·8	919·9	
CPF 645	Y	920·0	0·0	916·2	−3·8	911·4	−8·6	905·5	−14·5	4·3	918·3	
AEI 763	Y	763·0–834·3	0·0	763·2–834·0	0·0	763·4–833·6	0·0	763·5–833·4	0·0	2·4	763·1–834·2	0·0
AEI 702	Y	716·8–833·9	0·0	716·9–833·5	0·0	716·9–833·3	0·0	717·0–833·1	0·0	1·5	716·8–833·8	0·0
AEI 666	Y	716·8–833·7	0·0	716·9–833·8	0·0	717·0–833·8	0·0	717·1–833·8	0·0	0·2	716·8–833·7	0·0
BEI 738	N	738·0–817·1	0·0	745·9–815·2	0·0	751·6–809·6	0·0	755·5–804·6	0·0	18·8	745·9–815·2	0·0
BEI 715	N	716·0–815·8	0·0	721·6–815·2	0·0	726·1–808·8	0·0	729·6–802·9	0·0	56·5	735·5–788·4	−11·6
BEI 674	N	DNP		DNP		DNP		DNP		82·3	DNP	
CEI 889	N	914·0–958·4	0·0	948·2–968·3	28·2	972·4–974·4	52·4	DNP		20·4	973·2–974·6	53·2
CEI 820	N	913·4–959·7	0·0	944·3–967·7	24·3	967·4–973·5	47·4	DNP		34·6	DNP	
CEI 711	N	923·5–945·7	3·5	932·7–951·6	12·7	941·3–957·2	21·3	949·4–962·6	29·4	11·9	934·3–952·6	14·3
CPI 897	Y	897·0–981·0	0·0	897·0–982·3	0·0	897·1–983·9	0·0	897·1–985·9	0·0	0·7	897·0–981·1	0·0
CPI 858	Y	891·4–980·4	0·0	891·1–982·2	0·0	890·6–984·4	0·0	890·1–987·4	0·0	0·0	891·4–980·4	0·0

Sim. mig. abbrev., simulated migmatite abbreviation; Peak *T* Kfs, Y (yes) if the mineral assemblage includes solid K-feldspar at peak temperature, N (no) otherwise; $T^{Peak}_{Estimate}$, estimate of the peak temperature based on T–X_{Leuco} phase diagrams (Fig. 8 and Supplementary Data Fig. A4): for simulated migmatites that crystallized in isolation, $T^{Peak}_{Estimate}$ is the precise temperature of the lower-temperature boundary of the peak-temperature mineral assemblage; for simulated migmatites that crystallized via the chemical interaction model, $T^{Peak}_{Estimate}$ is the range of temperatures bracketed by the peak-temperature assemblage field (in the former case, the peak-temperature mineral assemblage is the assemblage preserved and observed in the melanosome; in the latter case, the peak-temperature mineral assemblage must be inferred petrographically); ΔT^{Peak}, difference between $T^{Peak}_{Estimate}$ and the known peak temperature; X_{Leuco}, amount of leucosome relative to melanosome plus leucosome; DNP, the peak-temperature mineral assemblage does not plot in the T–X_{Leuco} phase diagram for the given amount of leucosome contamination.

for sampling migmatites and using phase diagrams to estimate peak and solidification temperatures for migmatites. We determine the optimal mineral assemblage field, the field (i.e. melanosome, leucosome, or peak-*T* assemblage field) in the phase diagram most likely to bracket the known peak *T* for a specific value of X_{Leuco}, called the optimal value of X_{Leuco}. The optimal value of X_{Leuco} indicates the most useful sample to collect from outcrop to constrain the peak *T*. The same analysis is then repeated for the known solidification temperature. Second, after developing these strategies, we utilize them to estimate the peak and solidification temperature from the phase diagram (Tables 4 and 5). An estimated temperature is the *T* range of the optimal mineral assemblage field at the optimal value of X_{Leuco}. Third, the T–X_{Leuco} diagrams are used to assess sensitivity to contamination. If a petrologist's goal is to sample only the melanosome, but the sample unintentionally or unavoidably contains a small amount of leucosome material, this is herein called leucosome contamination, measured as the wt % of leucosome material in the sample. Melanosome contamination is analogously the wt % of melanosome unintentionally incorporated in a sample intended to be entirely leucosome. Examination of the migmatite in Fig. 1b shows how difficult it may be in practice to sample only the melanosome or only the leucosome. To assess the effects of contamination, we again estimate the peak and solidification temperature from the T–X_{Leuco} phase diagram, but instead of using the optimal value of X_{Leuco}, we use the optimal value of X_{Leuco} contaminated with melanosome or leucosome (Tables 4 and 5).

Estimating the peak *T* of a heterogeneous migmatite

In every T–X_{Leuco} diagram except two, the peak assemblage field (a field that is either yellow or includes yellow stripes in Fig. 8 and Supplementary Data Fig. A4), on the left, 100 wt % melanosome axis, brackets the known peak *T* (red dashed line). This relationship must be the case for the IFC and IEC simulations, because the

Table 5: Solidification temperature estimates (in °C) for leucosome bulk-compositions with various amounts of melanosome contamination

Simulated migmatite abbreviation	T^{Solid}_{Known}	Amount of melanosome contamination (wt %)							
		0·0		1·0		4·0		10·0	
		$T^{Solid}_{Estimate}$	ΔT^{Solid}	$T^{Solid}_{Estimate}$	ΔT^{Solid}	$T^{Solid}_{Estimate}$	ΔT^{Solid}	$T^{Solid}_{Estimate}$	ΔT^{Solid}
AEE 750	750	750·0	0·0	770·2	20·2	792·1	42·1	794·1	44·1
AEE 647	647	647·0	0·0	689·0	42·0	701·8	54·8	701·7	54·7
AEE 632	632	632·0	0·0	687·6	55·6	700·2	68·2	700·1	68·1
BEE 720	720	720·0	0·0	729·5	9·5	739·1	19·1	758·2	38·2
BEE 645	645	645·0	0·0	699·1	54·1	706·3	61·3	706·1	61·1
BEE 639	639	639·0	0·0	703·8	64·8	703·5	64·5	703·4	64·4
CEE 888	888	882·0	−6·0	926·6	38·6	918·5	30·5	915·2	27·2
CEE 819	819	782·9	−36·1	810·3	−8·7	855·3	36·3	903·0	84·0
CEE 684	684	684·0	0·0	684·0	0·0	683·8	−0·2	683·6	−0·4
AFF 691	691	703·0	12·0	703·0	12·0	702·9	11·9	702·7	11·7
AFF 626	626	700·8	74·9	700·7	74·8	700·6	74·7	700·5	74·6
AFF 624	624	699·3	75·3	699·3	75·3	699·2	75·2	699·2	75·2
BFF 630	630	691·0	61·0	691·5	61·5	692·9	62·9	696·7	66·7
BFF 625	625	700·6	75·6	700·5	75·5	700·3	75·3	700·5	75·5
BFF 624	624	699·0	75·0	698·8	74·8	698·7	74·7	699·0	75·0
CFF 726	726	741·6	15·6	750·9	24·9	778·2	52·2	786·6	60·6
CFF 636	636	682·2	46·2	682·2	46·2	682·2	46·2	682·1	46·1
CFF 631	631	680·5	49·5	680·5	49·5	680·4	49·4	680·4	49·4
CPF 894	894	915·8	21·8	916·1	22·1	914·5	20·5	914·4	20·4
CPF 829	829	825·2	–3·8	835·0	6·0	860·3	31·3	904·1	75·1
CPF 645	645	742·5	97·5	752·2	107·2	780·6	135·6	791·4	146·4

T^{Solid}_{Known}, the known solidification temperature; $T^{Solid}_{Estimate}$, estimate of the solidification temperature based on the temperature of the solidus in T–X_{Leuco} phase diagrams (Fig. 8 and Supplementary Data Fig. A3); $\Delta T^{Solid} = T^{Solid}_{Estimate} - T^{Solid}_{Known}$.

melanosome domain (with $X_{Leuco} = 0$) attains the peak-T assemblage at peak T, then does not interact or react during cooling. This relationship is also the case for the CIC simulations, even though the melanosome and peak-T assemblages may differ owing to chemical interaction between the two domains during cooling and retrograde reactions. In one of the exceptional cases, the peak-T assemblage field plots only 3·5°C above the known peak T (CEI 711; Supplementary Data Fig. A4dd), well within the uncertainty of the phase diagram method. The other exceptional case is atypical because chemical interaction proceeded extensively during crystallization, to the point that the melanosome and leucosome reached identical chemical compositions but perhaps not textures (BEI 674; Supplementary Data Fig. A4aa). Consequently, the peak-T assemblage field is the optimal mineral assemblage field and $X_{Leuco} = 0$ is the optimal value of X_{Leuco} for estimating the peak T.

In T–X_{Leuco} diagrams calculated for CIC simulated migmatites, the width of the peak assemblage field ranges between 22 and 117°C for the examples given in Table 4, with a median of 82°C. For example, the peak assemblage field for BEI 715 spans 100°C (716·0–815·8°C) and for CEI 820 it spans 46°C (913·4–959·7°C); both place imprecise estimates on peak T (Fig. 8e and f).

In phase diagrams for migmatites simulated with an isolated crystallization process (IEC or IFC), precise T estimates are possible (Table 4 and Fig. 8a–d). In Fig. 8a–d, the green solidus line on the $X_{Leuco} = 0$ (100 wt % melanosome) axis of the T–X_{Leuco} diagrams coincides with the known peak T and forms the lower-T boundary of the peak assemblage field. The solidus for the melanosome-only composition must coincide with the peak T because the melanosome was simulated to have an infinitesimal amount of liquid at peak T. Although the peak-T assemblage field often ranges over several tens of degrees Celsius (e.g. AEE 647 has a range of 35°C from 800 to 835°C and CPF 645 has a range of 62°C from 920 to 982°C; Fig. 8a and d), the low-T boundary of the field coincides with the known peak T. Therefore, the peak T for all IFC and IEC simulated migmatites can be estimated precisely to a single value (Table 4) if the crystallization processes of the migmatite can be determined. If the segregation of melt and solids was not completely efficient, as assumed here, and some melt remained in the melanosome at peak T, the solidus would give a lower bound for the peak T and the peak-T assemblage field would bracket the peak T. Although it is not possible to determine the degree of leucosome–melt–melanosome interaction in an outcrop, different crystallization processes can potentially be distinguished by comparing the composition of minerals in the melanosome and leucosome, especially Pl, as discussed above.

The effect of leucosome contamination on peak-*T* estimates

To understand the effect of contamination of melanosome by leucosome, Table 4 records estimates of the peak T derived from the T–X_{Leuco} diagrams for 10, 20, and 30 wt % leucosome contamination. It also lists the peak T for a bulk composition that has the actual leucosome:melanosome ratio generated in the crystallization

simulation (shown by the vertical black dashed lines in Fig. 8 and Supplementary Data Fig. A4). These estimates address the problem of collecting a 'representative' sample of a heterogeneous (simulated) migmatite from an outcrop that includes both leucosome and melanosome (e.g. all of the material in Fig. 1), without trying to separate the two components.

Peak-*T* estimates become less accurate for the simulated migmatites as leucosome is incorporated into the sample (i.e. as X_{Leuco} increases). With 10 wt % leucosome contamination, estimates are erroneous by −18 to +28°C, increasing to −50 to +49°C with 30 wt % contamination. For some simulated migmatites, typically those that do not have Kfs as a stable phase in the peak assemblage and involving a high proportion of leucosome (e.g. CEE 684; Figs 3j and 6g; CEI 820; Supplementary Data Fig. A1e–h), the peak assemblage field pinches out to the right (e.g. Fig. 8b and f); consequently, the peak assemblage field does not appear on the diagram for intermediate and large values of X_{Leuco}, hence peak *T* cannot be estimated for such values of X_{Leuco}. The number of peak-*T* assemblages that cannot be plotted increases from four out of 32 for 10 wt % contamination to eight out of 32 with 30 wt % contamination. For simulated migmatites sampled with the amount of melanosome and leucosome predicted by the crystallization simulations, the peak assemblage does not plot for eight of the 32 migmatites and no peak-*T* estimate can be made. For the other 24 migmatites, errors of −24 to +53°C were found.

A simulated migmatite is most susceptible to an erroneous peak-*T* estimate owing to leucosome contamination if its phase diagram has a sloping phase assemblage boundary on the edge of the peak-*T* mineral assemblage field. In particular, sloping solidi and Kfs-out phase boundaries cause erroneous peak-*T* estimates. For each simulated migmatite that underwent IFC or IEC, the solidus temperature on the *T*–X_{Leuco} diagram decreases with increasing leucosome contamination as the bulk composition becomes less residual (e.g. Fig. 8a). Estimating the peak *T* to be the temperature of the solidus leads to estimates that are lower than the known peak *T* (Table 4). For example, the peak-*T* estimate for AEE 647 decreases from 791°C with 10 wt % leucosome contamination, an error of 9°C below the 800°C peak *T*, to 772°C with 30 wt % leucosome contamination, 28°C below the peak *T* (Fig. 8a). In most cases in which Kfs is part of the peak assemblage, the peak assemblage field brackets the known peak *T* (Fig. 8a, c and d). If leucosome contamination is suspected, the peak *T* should be estimated as the range of the entire peak assemblage field.

Kfs-out phase boundaries have both positive and negative slopes (e.g. Fig. 8b, e and f). Incorporating the potassic leucosome into the bulk composition reduces the size of the Kfs-free assemblage field. Errors in peak-*T* estimates occur for simulated migmatites without Kfs as a stable phase at peak *T* because the Kfs-free field shifts and shrinks as X_{Leuco} increases. In the case of BEI 715, the Kfs-out phase boundary has a negative slope in the phase diagram (Fig. 8e), and for leucosome contamination corresponding to X_{Leuco} of 0·18 or greater, the peak *T* is underestimated by the peak-*T* mineral assemblage. Peak *T* is overestimated for CEE 684 because the Kfs-out phase boundary has a positive slope in the phase diagram (Fig. 8b). With only 5 wt % leucosome contamination, the peak-*T* estimate is erroneously high by 11°C. With over 38 wt % leucosome contamination, the peak-*T* assemblage field pinches out. If 39 wt % or more of a sample collected from this (simulated) outcrop consists of leucosome, the peak-*T* assemblage does not appear in the phase diagram, and the peak *T* cannot be estimated using the techniques discussed here. Similar to Kfs-out phase boundaries, Pl-out phase boundaries are sloped (e.g. Fig. 8b, e and f). Similar to migmatites in which all Kfs was consumed during melting, leucosome contamination may cause errors in peak-*T* estimates for migmatites in which all Pl was consumed during melting. If Kfs or Pl is interpreted to have been absent at peak *T*, and leucosome contamination is suspected, a conservative approach to estimating the peak *T* is to consider the temperature spanned by both the peak-*T* assemblage field and the peak-*T* assemblage field plus the feldspar that was not stable at peak conditions. Using CEE 684 again as an example, the combination of both the peak-*T* assemblage and the peak-*T* assemblage plus Kfs (Kfs + Crd + Spl + Grt + Sil + Pl + Ilm + Qtz + Liq) fields bracket the known peak *T* (Fig. 8b). The peak-*T* estimate is less precise with this approach, but it may allow an accurate estimate to be made when there is leucosome contamination. This conservative approach is also useful if it is unclear whether Kfs (or Pl) was completely absent at peak *T* and all Kfs crystallized during cooling, or some Kfs remained at peak conditions. By considering both options, both Kfs-present and Kfs-absent at peak *T*, the peak-*T* estimate brackets the known peak *T*, but at the expense of higher precision.

In summary, for all crystallization processes, errors in peak-*T* estimates induced by contamination of melanosome by leucosome are most likely if Kfs or Pl were not stable in the melanosome at peak *T*. The reason is that feldspar-absent peak-*T* mineral assemblage fields, although stable for the melanosome composition, are not stable for the feldspar-rich leucosome composition, and therefore they shrink as X_{Leuco} increases. For simulations involving crystallization of melt in isolation, peak-*T* estimates typically become erroneously low as the degree of leucosome contamination increases because the solidus temperature decreases. All errors owing to leucosome contamination increase with the degree of contamination.

Estimating the solidification temperature of a heterogeneous migmatite

Estimating the solidification temperature of a migmatite is difficult because it depends so strongly on the

crystallization process, as well as the possibility of physically induced melt loss. In most of our simulations, crystallization stops above the solidus owing to retrograde or prograde melt loss, so the solidification temperature relates to the T of melt loss. For crystallization simulations involving chemical interaction with and without melt loss, it is relatively straightforward to determine the solidification temperature; however, for the majority of crystallization simulations involving an isolated crystallization process with melt loss, it is only possible to constrain the solidification temperature within limits.

For crystallization simulations involving physical segregation of melt and residuum, but chemical interaction between them, the solidus coincides with the known solidification temperature on both the $X_{Leuco} = 0$ and $X_{Leuco} = 1$ (100 wt % leucosome) axes (e.g. Fig. 8e and f). Based on the shape of the solidus, either melanosome or leucosome may be sampled to recover the solidification temperature. The curved shape of the solidus is a result of the approximations made in the CIC model; had the simulated melanosome and leucosome been truly in equilibrium, the solidus would be a straight horizontal line on the T–X_{Leuco} diagram. Therefore, the solidus of any sample of leucosome and melanosome would coincide with, and could be used to constrain, the solidification temperature. The relative ease of determining the solidification temperature, assuming true equilibrium crystallization, has been utilized in several studies (e.g. Indares *et al.*, 2008; Guilmette *et al.*, 2011; Groppo *et al.*, 2012, 2013); however, our study shows that the crystallization processes must be considered with care.

For crystallization simulations involving IEC, the solidus on the $X_{Leuco} = 1$ axis coincides with the known solidification temperature, as expected for an equilibrium system (e.g. Fig. 8a and b). Therefore, the solidification temperature can be accurately estimated as the T of the solidus in a phase diagram calculated with the leucosome composition. However, in most cases, the solidus has a steep slope near the $X_{Leuco} = 1$ axis (e.g. Fig. 8a), meaning that estimating the solidification temperature using this method is acutely sensitive to melanosome contamination. The errors that arise with 1, 4, and 10 wt % melanosome contamination are given in Table 5 and range from −9°C to +84°C, relative to the known solidification temperature.

For crystallization simulations involving IFC, the T–X_{Leuco} phase diagrams are similar to the T–X_{Leuco} diagrams involving IEC. However, no phase boundary or mineral assemblage field consistently constrains the known solidification temperature; in particular, the solidus plots at a higher T than the known solidification temperature for all values of X_{Leuco} because the aggregate leucosome composition was not in equilibrium with the final melt in the system. In the T–X_{Leuco} diagrams, the solidus intersects the $X_{Leuco} = 1$ axis at T greater than the known solidification temperature by 12–98°C (Table 5; Fig. 8c and d). Because the leucosome formed from IFC, it consists of minerals that crystallized at the known solidification temperature and above, so the solidus corresponding to the bulk leucosome composition plots above the known solidification temperature. CPF 829 is exceptional because the solidus at $X_{Leuco} = 1$ plots 4°C below the known solidification temperature (Supplementary Data Fig. A4t). This atypical behaviour is a result of the predicted prograde reaction Liq + Grt + Sil = Crd + Spl + Kfs + Pl + Qtz that consumes melt and gives the solidus an unusually complex shape near the $X_{Leuco} = 1$ axis (Supplementary Data Fig. A4t). The solidus in a phase diagram calculated with the leucosome composition gives a maximum-T constraint on the solidification temperature for the vast majority of simulated migmatites.

The significance of accurate bulk-rock H_2O analyses

Perhaps the most important chemical component in migmatites from a modelling perspective is the bulk-rock H_2O content, because it affects reactions involving initial melting and final solidification, as well as higher-T reactions (White *et al.*, 2001). Consequently, bulk-rock H_2O content should be measured as part of geochemical analysis. Rocks that have undergone subsolidus retrograde hydration (alteration) should be avoided. Techniques that directly measure bound water (H_2O^+) are best, such as the Karl Fischer titration or analysis with a C–N–H elemental analyser (e.g. Potts, 1987). Sensitivity analysis, in the form of a T–m_{H2O} diagram (White *et al.*, 2001; Taylor *et al.*, 2010; Korhonen *et al.*, 2011), allows for quantification of the uncertainty in peak and solidification temperature estimates owing to uncertainty in the H_2O analysis.

Melt migration and the relationship between leucosome and melanosome

If melt separates from the source, it has the potential to form a melt-filled vein network (Waff & Bulau, 1979; Toramaru & Fujii, 1986; Holness *et al.*, 2011). Lithostatic and tectonic stresses have the potential to drive the migration of the melt through the network (Simakin & Talbot, 2001). As a result, a melt may come to rest and crystallize next to a residuum with a different bulk composition compared with the residuum from which it was derived. Migmatite terrains have been identified where relatively small leucosomes form connected networks, suggesting relatively pervasive flow through a thin network of veins (Morfin *et al.*, 2014, and references therein).

In cases in which the leucosome and melanosome are genetically unrelated, they should, in general, be more chemically dissimilar to the melanosome–leucosome pairs considered in the T–X_{Leuco} diagrams here (Fig. 8; Supplementary Data Fig. A4). Contamination of a melanosome composition with a chemically dissimilar leucosome will probably lead to even greater errors in peak-T estimates. The general strategy suggested here, to sample the melanosome exclusively if interested in the peak T, should be even more important in this case.

Working with phase diagrams for heterogeneous pelitic migmatites

Recognizing that migmatites may have lost melt and that the leucosome and melanosome may or may not have evolved together in equilibrium, we have determined the best approach to estimate the peak T of metamorphism and the solidification temperature from standard isochemical equilibrium phase assemblage diagrams (pseudosections) calculated from major element compositions of rock samples collected from outcrop. The peak T can be accurately estimated from a phase diagram calculated with the composition of the melanosome, if the mineral assemblage at peak T can be inferred from petrographic observations. In a minority of cases, contaminating a melanosome sample with leucosome leads to inaccurate peak-T estimates (by -25 to $+50^{\circ}$C), or the inability to estimate the peak T: the worst case occurs if a phase that is abundant in the leucosome (e.g. feldspar) was completely consumed during melting, leaving a melanosome devoid of that mineral. In melanosome samples contaminated by leucosome, inferring the peak-T assemblage may be difficult; however, less precise but accurate peak-T estimates may be made by considering the two (or more) different possible inferred peak-T assemblages. Accurately constraining the solidification temperature is generally possible only if the leucosome and melanosome have maintained chemical communication during crystallization; it may also be possible for a sample of leucosome that crystallized in isolated equilibrium if it is completely uncontaminated with melanosome. In both cases, constraining the solidification temperature requires an accurate measurement of the lattice-bound H_2O in the bulk-rock composition. Because the components sampled for thermodynamic analysis (melanosome and/or leucosome) can significantly influence T estimates, future studies of migmatites should describe what was sampled and analysed.

ACKNOWLEDGEMENTS

We thank Doug Tinkham for his inexhaustible assistance with Theriak/Domino. The speakers and participants of the European Intensive Seminars of Petrology (EURISPET) on High-temperature Metamorphism and Crustal Melting (University of Padua, Italy, 2010) are thanked for numerous insightful discussions and talks. We thank T. Chacko, B. Guest, and R. Nair for reviewing an earlier version of the paper. The paper saw significant improvement owing to constructive and insightful reviews by N. Daczko, I. Fitzsimons, E. Sawyer and C. Yakymchuk.

FUNDING

This work was supported by the Natural Sciences and Engineering Research Council of Canada (NSERC) (Discovery Grant 037233 to D.R.M.P.). We also acknowledge the following sources of support to B.M.K.: an NSERC Alexander Graham Bell Canada Graduate Scholarship, a W. Garfield Weston Award for Northern Research (Doctoral), and an Izaak Walton Killam Pre-Doctoral Scholarship.

SUPPLEMENTARY DATA

Supplementary data for this paper are available at *Journal of Petrology* online.

REFERENCES

Acosta-Vigil, A., London, D. & Morgan, G. B. (2006). Experiments on the kinetics of partial melting of a leucogranite at 200 MPa H_2O and 690–800°C: compositional variability of melts during the onset of H_2O-saturated crustal anatexis. *Contributions to Mineralogy and Petrology* **151**, 539–557.

Ague, J. J. (1991). Evidence for major mass transfer and volume strain during regional metamorphism of pelites. *Geology* **19**, 855–858.

Ashworth, J. R. (1975). Staurolite at anomalously high grade. *Contributions to Mineralogy and Petrology* **53**, 281–291.

Bartoli, O., Cesare, B., Poli, S., Bodnar, R. J., Acosta-Vigil, A., Frezzotti, M. L. & Meli, S. (2013). Recovering the composition of melt and the fluid regime at the onset of crustal anatexis and S-type granite formation. *Geology* **41**, 115–118.

Benard, F., Moutou, P. & Pichavant, M. (1985). Phase relations of tourmaline leucogranites and the significance of tourmaline in silicic magmas. *Journal of Geology* **93**, 271–291.

Boger, S. D., White, R. W. & Schulte, B. (2012). The importance of iron speciation (Fe^{+2}/Fe^{+3}) in determining mineral assemblages: an example from the high-grade aluminous metapelites of southeastern Madagascar. *Journal of Metamorphic Geology* **30**, 997–1018.

Braga, R. & Massonne, H.-J. (2011). H_2O content of deep-seated orogenic continental crust: the Ulten Zone, Italian Alps. *International Geology Review* **54**, 633–641.

Brown, C. R., Yakymchuk, C., Brown, M., Fanning, C. M., Korhonen, F. J., Piccoli, P. M. & Siddoway, C. S. (2016). From source to sink: petrogenesis of Cretaceous anatectic granites from the Fosdick migmatite–granite complex, West Antarctica. *Journal of Petrology* **57**, 1241–1278.

Brown, M. (1994). The generation, segregation, ascent and emplacement of granite magma: the migmatite-to-crustally-derived granite connection in thickened orogens. *Earth-Science Reviews* **36**, 83–130.

Brown, M. (2002). Retrograde processes in migmatites and granulites revisited. *Journal of Metamorphic Geology* **20**, 25–40.

Brown, M. (2007). Crustal melting and melt extraction, ascent and emplacement in orogens: mechanisms and consequences. *Journal of the Geological Society, London* **164**, 709–730.

Brown, M. (2013). Granite: From genesis to emplacement. *Geological Society of America Bulletin* **125**, 1079–1113.

Brown, M. & Korhonen, F. J. (2009). Some remarks on melting and extreme metamorphism of crustal rocks. In: Gupta, A. K. & Dasgupta, S. (eds) *Physics and Chemistry of the Earth's Interior*. Springer, pp. 67–87.

Brown, M., Korhonen, F. J. & Siddoway, C. S. (2011). Organizing melt flow through the crust. *Elements* **7**, 261–266.

Burda, J. & Gawęda, A. (2009). Shear-influenced partial melting in the Western Tatra metamorphic complex: Geochemistry and geochronology. *Lithos* **110**, 373–385.

Cameron, E. M. & Garrels, R. M. (1980). Geochemical compositions of some Precambrian shales from the Canadian Shield. *Chemical Geology* **28**, 181–197.

Carson, C. J., Powell, R., Wilson, C. J. L. & Dirks, P. H. G. M. (1997). Partial melting during tectonic exhumation of a granulite terrane: an example from the Larsemann Hills, East Antarctica. *Journal of Metamorphic Geology* **15**, 105–126.

Carvalho, B. B., Sawyer, E. W. & Janasi, V. A. (2016). Crustal reworking in a shear zone: transformation of metagranite to migmatite. *Journal of Metamorphic Geology* **34**, 237–264.

Castro, A., Patiño Douce, A. E., Corretgé, L. G., de la Rosa, J. D., El-Biad, M. & El-Hmidi, H. (1999). Origin of peraluminous granites and granodiorites, Iberian massif, Spain: an experimental test of granite petrogenesis. *Contributions to Mineralogy and Petrology* **135**, 255–276.

Chorlton, L. B. & Martin, R. F. (1978). Effect of boron on the granite solidus. *Canadian Mineralogist* **16**, 239–244.

Coggon, R. & Holland, T. J. B. (2002). Mixing properties of phengitic micas and revised garnet–phengite thermobarometers. *Journal of Metamorphic Geology* **20**, 683–696.

Connolly, J. A. D. & Cesare, B. (1993). C–O–H–S fluid composition and oxygen fugacity in graphitic metapelites. *Journal of Metamorphic Geology B* **11**, 379–388.

Cross, W., Iddings, J. P., Pirsson, L. V. & Washington, H. S. (1903). *Quantitative Classification of Igneous Rocks*. University of Chicago Press.

Cruciani, G., Franceschelli, M., Jung, S., Puxeddu, M. & Utzeri, D. (2008). Amphibole-bearing migmatites from the Variscan Belt of NE Sardinia, Italy: partial melting of mid-Ordovician igneous sources. *Lithos* **105**, 208–224.

Daczko, N. R. & Halpin, J. A. (2009). Evidence for melt migration enhancing recrystallization of metastable assemblages in mafic lower crust, Fiordland, New Zealand. *Journal of Metamorphic Geology* **27**, 167–185.

de Capitani, C. & Brown, T. H. (1987). The computation of chemical equilibrium in complex systems containing non-ideal solutions. *Geochimica et Cosmochimica Acta* **51**, 2639–2652.

de Capitani, C. & Petrakakis, K. (2010). The computation of equilibrium assemblage diagrams with Theriak/Domino software. *American Mineralogist* **95**, 1006–1016.

Diener, J. F. A. & Fagereng, Å. (2014). The influence of melting and melt drainage on crustal rheology during orogenesis. *Journal of Geophysical Research: Solid Earth* **119**, 6193–6210.

Dini, A., Gianelli, G., Puxeddu, M. & Ruggieri, G. (2005). Origin and evolution of Pliocene–Pleistocene granites from the Larderello geothermal field (Tuscan Magmatic Province, Italy). *Lithos* **81**, 1–31.

Droop, G. T. R. & Brodie, K. H. (2012). Anatectic melt volumes in the thermal aureole of the Etive Complex, Scotland: the roles of fluid-present and fluid-absent melting. *Journal of Metamorphic Geology* **30**, 843–864.

Ellis, D. J. & Obata, M. (1992). Migmatite and melt segregation at Cooma, New South Wales. *Transactions of the Royal Society of Edinburgh: Earth Sciences* **83**, 95–106.

Fitzsimons, I. C. W. & Harley, S. L. (1994). The influence of retrograde cation exchange on granulite *P–T* estimates and a convergence technique for the recovery of peak metamorphic conditions. *Journal of Petrology* **35**, 543–576.

Fourcade, S., Martin, H. & de Brémond d'Ars, J. (1992). Chemical exchange in migmatites during cooling. *Lithos* **28**, 43–53.

Frost, B. R. & Chacko, T. (1989). The granulite uncertainty principle: Limitations on thermobarometry in granulites. *Journal of Geology* **97**, 435–450.

Frost, B. R., Barnes, C. G., Collins, W. J., Arculus, R. J., Ellis, D. J. & Frost, C. D. (2001). A geochemical classification for granitic rocks. *Journal of Petrology* **42**, 2033–2048.

Genier, F., Bussy, F., Epard, J.-L. & Baumgartner, L. (2008). Water-assisted migmatization of metagraywackes in a Variscan shear zone, Aiguilles-Rouges massif, western Alps. *Lithos* **102**, 575–597.

Gromet, L. P., Haskin, L. A., Korotev, R. L. & Dymek, R. F. (1984). The 'North American shale composite': its compilation, major and trace element characteristics. *Geochimica et Cosmochimica Acta* **48**, 2469–2482.

Groppo, C., Rolfo, F. & Indares, A. (2012). Partial melting in the Higher Himalayan Crystallines of eastern Nepal: the effect of decompression and implications for the 'channel flow' model. *Journal of Petrology* **53**, 1057–1088.

Groppo, C., Rolfo, F. & Mosca, P. (2013). The cordierite-bearing anatectic rocks of the higher Himalayan crystallines (eastern Nepal): low-pressure anatexis, melt productivity, melt loss and the preservation of cordierite. *Journal of Metamorphic Geology* **31**, 187–204.

Guernina, S. & Sawyer, E. W. (2003). Large-scale melt-depletion in granulite terranes: an example from the Archean Ashuanipi Subprovince of Quebec. *Journal of Metamorphic Geology* **21**, 181–201.

Guilmette, C., Indares, A. & Hébert, R. (2011). High-pressure anatectic paragneisses from the Namche Barwa, Eastern Himalayan Syntaxis: textural evidence for partial melting, phase equilibria modeling and tectonic implications. *Lithos* **124**, 66–81.

Gupta, L. N. & Johannes, W. (1982). Petrogenesis of a stromatic migmatite (Nelaug, southern Norway). *Journal of Petrology* **23**, 548–567.

Hamilton, B. M., Pattison, D. R. M., Sanborn-Barrie, M. & Young, M. D. (2012). Preliminary characterisation of metamorphism on Cumberland Peninsula, Baffin Island, Nunavut. *Geological Survey of Canada, Current Research* **2012-9**, 1–17.

Harris, N. B. W., Caddick, M., Kosler, J., Goswami, S., Vance, D. & Tindle, A. G. (2004). The pressure–temperature–time path of migmatites from the Sikkim Himalaya. *Journal of Metamorphic Geology* **22**, 249–264.

Holland, T. J. B. & Powell, R. (1998). An internally consistent thermodynamic data set for phases of petrological interest. *Journal of Metamorphic Geology* **16**, 309–343.

Holland, T. J. B. & Powell, R. (2001). Calculation of phase relations involving haplogranitic melts using an internally consistent thermodynamic dataset. *Journal of Petrology* **42**, 673–683.

Holland, T. & Powell, R. (2003). Activity–composition relations for phases in petrological calculations: an asymmetric multicomponent formulation. *Contributions to Mineralogy and Petrology* **145**, 492–501.

Holness, M. B. & Sawyer, E. W. (2008). On the pseudomorphing of melt-filled pores during the crystallization of migmatites. *Journal of Petrology* **49**, 1343–1363.

Holness, M. B., Cesare, B. & Sawyer, E. W. (2011). Melted rocks under the microscope: microstructures and their interpretation. *Elements* **7**, 247–252.

Indares, A., White, R. W. & Powell, R. (2008). Phase equilibria modelling of kyanite-bearing anatectic paragneisses from the central Grenville Province. *Journal of Metamorphic Geology* **26**, 815–836.

Jamieson, R. A. & Beaumont, C. (2013). On the origin of orogens. *Geological Society of America Bulletin* **125**, 1671–1702.

Johannes, W. (1978). Melting of plagioclase in the system Ab–An–H_2O and Qz–Ab–An–H_2O at $P_{H2O} = 5$ kbars, an equilibrium problem. *Contributions to Mineralogy and Petrology* **66**, 295–303.

Johannes, W. (1980). Metastable melting in the granite system Qz–Or–Ab–An–H_2O. *Contributions to Mineralogy and Petrology* **72**, 73–80.

Johannes, W. (1984). Beginning of melting in the granite system Qz–Or–Ab–An–H_2O. *Contributions to Mineralogy and Petrology* **86**, 264–273.

Johannes, W. & Gupta, L. N. (1982). Origin and evolution of a migmatite. *Contributions to Mineralogy and Petrology* **79**, 114–123.

Johannes, W., Holtz, F. & Möller, P. (1995). REE distribution in some layered migmatites: constraints on their petrogenesis. *Lithos* **35**, 139–152.

Johannes, W., Ehlers, C., Kriegsman, L. M. & Mengel, K. (2003). The link between migmatites and S-type granites in the Turku area, southern Finland. *Lithos* **68**, 69–90.

Johnson, T. E., Hudson, N. F. C. & Droop, G. T. R. (2001). Partial melting in the Inzie Head gneisses: the role of water and a petrogenetic grid in KFMASH applicable to anatectic pelitic migmatites. *Journal of Metamorphic Geology* **19**, 99–118.

Johnson, T. E., Hudson, N. F. C. & Droop, G. T. R. (2003). Evidence for a genetic granite–migmatite link in the Dalradian of NE Scotland. *Journal of the Geological Society, London* **160**, 447–457.

Jung, S., Mezger, K., Masberg, P., Hoffer, E. & Hoernes, S. (1998). Petrology of an intrusion-related high-grade migmatite: implications for partial melting of metasedimentary rocks and leucosome-forming processes. *Journal of Metamorphic Geology* **16**, 425–445.

Jung, S., Hoernes, S. & Mezger, K. (2000). Geochronology and petrology of migmatites from the Proterozoic Damara Belt—importance of episodic fluid-present disequilibrium melting and consequences for granite petrology. *Lithos* **51**, 153–179.

Kelsey, D. E. & Hand, M. (2015). On ultrahigh temperature crustal metamorphism: phase equilibria, trace element thermometry, bulk composition, heat sources, timescales and tectonic settings. *Geoscience Frontiers* **6**, 311–356.

Korhonen, F. J., Saw, A. K., Clark, C., Brown, M. & Bhattacharya, S. (2011). New constraints on UHT metamorphism in the Eastern Ghats Province through the application of phase equilibria modelling and *in situ* geochronology. *Gondwana Research* **20**, 764–781.

Kriegsman, L. M. (2001). Partial melting, partial melt extraction and partial back reaction in anatectic migmatites. *Lithos* **56**, 75–96.

Le Maitre, R. W. (ed.) (2002). Igneous Rocks: A Classification and Glossary of Terms*, 2nd edn*. Cambridge University Press.

Marchildon, N. & Brown, M. (2001). Melt segregation in late syn-tectonic anatectic migmatites: an example from the Onawa contact aureole, Maine, USA. *Physics and Chemistry of the Earth, Part A* **26**, 225–229.

Mehnert, K. R. (1968). *Migmatites and the Origin of Granitic Rocks*. Elsevier.

Milord, I., Sawyer, E. W. & Brown, M. (2001). Formation of diatexite migmatite and granite magma during anatexis of semi-pelitic metasedimentary rocks: an example from St. Malo, France. *Journal of Petrology* **42**, 487–505.

Misch, P. (1968). Plagioclase compositions and non-anatectic origin of migmatitic gneisses in Northern Cascade mountains of Washington State. *Contributions to Mineralogy and Petrology* **17**, 1–70.

Misiti, V., Tecce, F. & Gaeta, M. (2005). Fluids in low-pressure migmatites: a fluid inclusion study of rocks from the Gennargentu Igneous Complex (Sardinia, Italy). *Mineralogy and Petrology* **85**, 253–268.

Morfin, S., Sawyer, E. W. & Bandyayera, D. (2014). The geochemical signature of a felsic injection complex in the continental crust: Opinaca Subprovince, Quebec. *Lithos* **196–197**, 339–355.

Nabelek, P. I. (1999). Trace element distribution among rock-forming minerals in Black Hills migmatites, South Dakota: a case for solid-state equilibrium. *American Mineralogist* **84**, 1256–1269.

Nabelek, P. I., Russ-Nabelek, C. & Denison, J. R. (1992). The generation and crystallization conditions of the Proterozoic Harney Peak Leucogranite, Black Hills, South Dakota, USA: Petrologic and geochemical constraints. *Contributions to Mineralogy and Petrology* **110**, 173–191.

Nair, R. & Chacko, T. (2002). Fluid-absent melting of high-grade semi-pelites: *P–T* constraints on orthopyroxene formation and implications for granulite genesis. *Journal of Petrology* **43**, 2121–2142.

Nichols, G. T., Berry, R. F. & Green, D. H. (1992). Internally consistent gahnitic spinel–cordierite–garnet equilibria in the FMASHZn system: geothermobarometry and applications. *Contributions to Mineralogy and Petrology* **111**, 362–377.

Nyman, M. W., Pattison, D. R. M. & Ghent, E. D. (1995). Melt extraction during formation of K-feldspar + sillimanite migmatites, west of Revelstoke, British Columbia. *Journal of Petrology* **36**, 351–372.

Obata, M., Yoshimura, Y., Nagakawa, K., Odawara, S. & Osanai, Y. (1994). Crustal anatexis and melt migrations in the Higo metamorphic terrane, west–central Kyushu, Kumamoto, Japan. *Lithos* **32**, 135–147.

Otamendi, J. E. & Patiño Douce, A. E. (2001). Partial melting of aluminous metagreywackes in the northern Sierra de Comechingones, central Argentina. *Journal of Petrology* **42**, 1751–1772.

Palin, R. M., Weller, O. M., Waters, D. J. & Dyck, B. (2016). Quantifying geological uncertainty in metamorphic phase equilibria modelling; a Monte Carlo assessment and implications for tectonic interpretations. *Geoscience Frontiers* **7**, 591–607.

Patiño Douce, A. E. & Harris, N. (1998). Experimental constraints on Himalayan anatexis. *Journal of Petrology* **39**, 689–710.

Patiño Douce, A. E. & Johnston, A. D. (1991). Phase equilibria and melt productivity in the pelitic system: implications for the origin of peraluminous granitoids and aluminous granulites. *Contributions to Mineralogy and Petrology* **107**, 202–218.

Pattison, D. R. M. (1987). Variations in Mg/(Mg + Fe), F, and (Fe,Mg)Si = 2Al in pelitic minerals in the Ballachulish thermal aureole, Scotland. *American Mineralogist* **72**, 255–272.

Pattison, D. R. M. & Bégin, N. J. (1994). Zoning patterns in orthopyroxene and garnet in granulites: implications for geothermometry. *Journal of Metamorphic Geology* **12**, 387–410.

Peterson, J. W., Chacko, T. & Kuehner, S. M. (1991). The effects of fluorine on the vapor-absent melting of phlogopite + quartz: implications for deep-crustal processes. *American Mineralogist* **76**, 470–476.

Potts, P. J. (1987). *A Handbook of Silicate Rock Analysis*. Springer.

Powell, R. (1983). Processes in granulite-facies metamorphism. In: Atherton,M. P. & Gribble, C. D. (eds) *Migmatites, Melting and Metamorphism*. Shiva, pp. 127–139.

Powell, R. & Downes, J. (1990). Garnet porphyroblast-bearing leucosomes in metapelites: mechanisms, phase diagrams, and an example from Broken Hill, Australia. In: Ashworth, J. R. & Brown, M. (eds) *High-temperature Metamorphism and Crustal Anatexis*. Unwin Hyman, pp. 105–123.

Powell, R. & Holland, T. J. B. (1988). An internally consistent thermodynamic dataset with uncertainties and correlations: 3. Applications to geobarometry, worked examples and a computer program. *Journal of Metamorphic Geology* **6**, 173–204.

Powell, R. & Holland, T. (1999). Relating formulations of the thermodynamics of mineral solid solutions: activity modeling of pyroxenes, amphiboles, and micas. *American Mineralogist* **84**, 1–14.

Powell, R. & Holland, T. J. B. (2008). On thermobarometry. *Journal of Metamorphic Geology* **26**, 155–179.

Pressley, R. A. & Brown, M. (1999). The Phillips pluton, Maine, USA: evidence of heterogeneous crustal sources and implications for granite ascent and emplacement mechanisms in convergent orogens. *Lithos* **46**, 335–366.

Rabinowicz, M. & Vigneresse, J.-L. (2004). Melt segregation under compaction and shear channeling: Application to granitic magma segregation in a continental crust. *Journal of Geophysical Research: Solid Earth* **109**, B04407.

Redler, C., White, R. W. & Johnson, T. E. (2013). Migmatites in the Ivrea Zone (NW Italy): constraints on partial melting and melt loss in metasedimentary rocks from Val Strona di Omegna. *Lithos* **175–176**, 40–53.

Rosenberg, C. L. & Handy, M. R. (2001). Mechanisms and orientation of melt segregation paths during pure shearing of a partially molten rock analog (norcamphor–benzamide). *Journal of Structural Geology* **23**, 1917–1932.

Rosenberg, C. L. & Handy, M. R. (2005). Experimental deformation of partially melted granite revisited: implications for the continental crust. *Journal of Metamorphic Geology* **23**, 19–28.

Rutter, E. R. & Mecklenburgh, J. (2006). The extraction of melt from crustal protoliths and the flow behavior of partially molten crustal rocks: an experimental perspective. In: Brown, M. & Rushmer, T. (eds) *Evolution and Differentiation of the Continental Crust*. Cambridge University Press, pp. 384–429.

Sanborn-Barrie, M., Young, M., Keim, R. & Hamilton, B. (2013). Geology, Sunneshine Fiord, Baffin Island, Nunavut. *Geological Survey of Canada, Canadian Geoscience Map 6* (preliminary), scale 1:100 000.

Sawyer, E. W. (1987). The role of partial melting and fractional crystallization in determining discordant migmatite leucosome compositions. *Journal of Petrology* **28**, 445–473.

Sawyer, E. W. (1994). Melt segregation in the continental crust. *Geology* **22**, 1019–1022.

Sawyer, E. W. (2008a). *Atlas of Migmatites. Canadian Mineralogist, Special Publication*, **9**.

Sawyer, E. W. (2008b). Identifying the parts of migmatites in the field. In: Sawyer, E. W. & Brown, M. (eds) *Working with Migmatites. Mineralogical Association of Canada, Short Course Series* **38**, 29–36.

Sawyer, E. W. (2014). The inception and growth of leucosomes: microstructure at the start of melt segregation in migmatites. *Journal of Metamorphic Geology* **32**, 695–712.

Sawyer, E. W., Cesare, B. & Brown, M. (2011). When the continental crust melts. *Elements* **7**, 229–234.

Scaillet, B., Pichavant, M. & Roux, J. (1995). Experimental crystallization of leucogranite magmas. *Journal of Petrology* **36**, 663–705.

Simakin, A. & Talbot, C. (2001). Tectonic pumping of pervasive granitic melts. *Tectonophysics* **332**, 387–402.

Slagstad, T., Jamieson, R. A. & Culshaw, N. G. (2005). Formation, crystallization, and migration of melt in the mid-orogenic crust: Muskoka Domain migmatites, Grenville Province, Ontario. *Journal of Petrology* **46**, 893–919.

Solar, G. S. & Brown, M. (2001). Petrogenesis of migmatites in Maine, USA: possible source of peraluminous leucogranite in plutons?. *Journal of Petrology* **42**, 789–823.

Stevens, G., Villaros, A. & Moyen, J.-F. (2007). Selective peritectic garnet entrainment as the origin of geochemical diversity in S-type granites. *Geology* **35**, 9–12.

Stevenson, D. J. (1989). Spontaneous small-scale melt segregation in partial melts undergoing deformation. *Geophysical Research Letters* **16**, 1067–1070.

Stowell, H., Bulman, G., Tinkham, D. & Zuluaga, C. (2011). Garnet growth during crustal thickening in the Cascades Crystalline Core, Washington, USA. *Journal of Metamorphic Geology* **29**, 627–647.

Taylor, J., Stevens, G., Armstrong, R. & Kisters, A. F. M. (2010). Granulite facies anatexis in the Ancient Gneiss Complex, Swaziland, at 2·73 Ga: Mid-crustal metamorphic evidence for mantle heating of the Kaapvaal craton during Ventersdorp magmatism. *Precambrian Research* **177**, 88–102.

Taylor, J., Nicoli, G., Stevens, G., Frei, D. & Moyen, J.-F. (2014). The processes that control leucosome compositions in metasedimentary granulites: perspectives from the Southern Marginal Zone migmatites, Limpopo Belt, South Africa. *Journal of Metamorphic Geology* **32**, 713–742.

Taylor, S. R. & McLennan, S. M. (1985). *The Continental Crust: its Composition and Evolution*. Blackwell Scientific.

Tinkham, D. K., Zuluaga, C. A. & Stowell, H. H. (2001). Metapelite phase equilibria modeling in MnNCKFMASH; the effect of variable Al_2O_3 and MgO/(MgO + FeO) on mineral stability. *Geological Materials Research* **3**, 1–42.

Toramaru, A. & Fujii, N. (1986). Connectivity of melt phase in a partially molten peridotite. *Journal of Geophysical Research: Solid Earth* **91**, 9239–9252.

Touret, J. L. R. & Huizenga, J.-M. (2011). Fluids in granulites. In: van Reenen, D. D., Kramers, J. D., McCourt, S. & Perchuk, L. L. (eds) *Origin and Evolution of Precambrian High-Grade Gneiss Terranes, with Special Emphasis on the Limpopo Complex of Southern Africa. Geological Society of America, Memoirs* **207**, 25–37.

Vernon, R. H., Richards, S. W. & Collins, W. J. (2001). Migmatite–granite relationships: origin of the Cooma Granodiorite magma, Lachlan Fold Belt, Australia. *Physics and Chemistry of the Earth, Part A* **26**, 267–271.

Vielzeuf, D. & Holloway, J. R. (1988). Experimental determination of the fluid-absent melting relations in the pelitic system. *Contributions to Mineralogy and Petrology* **98**, 257–276.

Vigneresse, J. L., Barbey, P. & Cuney, M. (1996). Rheological transitions during partial melting and crystallization with application to felsic magma segregation and transfer. *Journal of Petrology* **37**, 1579–1600.

Villaros, A., Stevens, G. & Buick, I. S. (2009). Tracking S-type granite from source to emplacement: clues from garnet in the Cape Granite Suite. *Lithos* **112**, 217–235.

Waff, H. S. & Bulau, J. R. (1979). Equilibrium fluid distribution in an ultramafic partial melt under hydrostatic stress conditions. *Journal of Geophysical Research: Solid Earth* **84**, 6109–6114.

Wang, Y., Zhang, A., Fan, W., Zhao, G., Zhang, G., Zhang, Y., Zhang, F. & Li, S. (2011). Kwangsian crustal anatexis within the eastern South China Block: Geochemical, zircon U–Pb geochronological and Hf isotopic fingerprints from the gneissoid granites of Wugong and Wuyiunkai Domains. *Lithos* **127**, 239–260.

Ward, R., Stevens, G. & Kisters, A. (2008). Fluid and deformation induced partial melting and melt volumes in low-temperature granulite-facies metasediments, Damara Belt, Namibia. *Lithos* **105**, 253–271.

Waters, D. J. (1988). Partial melting and the formation of granulite facies assemblages in Namaqualand, South Africa. *Journal of Metamorphic Geology* **6**, 387–404.

Weinberg, R. F. & Hasalová, P. (2015). Water-fluxed melting of the continental crust: a review. *Lithos* **212–215**, 158–188.

White, R. W. & Powell, R. (2002). Melt loss and the preservation of granulite facies mineral assemblages. *Journal of Metamorphic Geology* **20**, 621–632.

White, R. W. & Powell, R. (2010). Retrograde melt–residue interaction and the formation of near-anhydrous leucosomes in migmatites. *Journal of Metamorphic Geology* **28**, 579–597.

White, R. W., Powell, R. Holland, T. J. B. & Worley, B. A. (2000). The effect of TiO_2 and Fe_2O_3 on metapelitic assemblages at

greenschist and amphibolite facies conditions: mineral equilibria calculations in the system K_2O–FeO–MgO–Al_2O_3–SiO_2–H_2O–TiO_2–Fe_2O_3. *Journal of Metamorphic Geology* **18**, 497–511.

White, R. W., Powell, R. & Holland, T. J. B. (2001). Calculation of partial melting equilibria in the system Na_2O–CaO–K_2O–FeO–MgO–Al_2O_3–SiO_2–H_2O (NCKFMASH). *Journal of Metamorphic Geology* **19**, 139–153.

White, R. W., Powell, R. & Clarke, G. L. (2002). The interpretation of reaction textures in Fe-rich metapelitic granulites of the Musgrave Block, central Australia: constraints from mineral equilibria calculations in the system K_2O–FeO–MgO–Al_2O_3–SiO_2–H_2O–TiO_2–Fe_2O_3. *Journal of Metamorphic Geology* **20**, 41–55.

White, R. W., Powell, R. & Clarke, G. L. (2003). Prograde metamorphic assemblage evolution during partial melting of metasedimentary rocks at low pressures: migmatites from Mt Stafford, central Australia. *Journal of Petrology* **44**, 1937–1960.

White, R. W., Powell, R. & Halpin, J. A. (2004). Spatially-focused melt formation in aluminous metapelites from Broken Hill, Australia. *Journal of Metamorphic Geology* **22**, 825–845.

White, R. W., Pomroy, N. E. & Powell, R. (2005). An *in situ* metatexite–diatexite transition in upper amphibolite facies rocks from Broken Hill, Australia. *Journal of Metamorphic Geology* **23**, 579–602.

White, R. W., Powell, R. & Holland, T. J. B. (2007). Progress relating to calculation of partial melting equilibria for metapelites. *Journal of Metamorphic Geology* **25**, 511–527.

Whitney, D. L. & Evans, B. W. (2010). Abbreviations for names of rock-forming minerals. *American Mineralogist* **95**, 185–187.

Whitney, D. L. & Irving, A. J. (1994). Origin of K-poor leucosomes in a metasedimentary migmatite complex by ultrametamorphism, syn-metamorphic magmatism and subsolidus processes. *Lithos* **32**, 173–192.

Wyllie, P. J. & Tuttle, O. F. (1961). Experimental investigation of silicate systems containing two volatile components; Part 2, The effects of NH_3 and HF, in addition to H_2O on the melting temperatures of albite and granite. *American Journal of Science* **259**, 128–143.

Yakymchuk, C. & Brown, M. (2014). Consequences of open-system melting in tectonics. *Journal of the Geological Society, London* **171**, 21–40.